Check for updates

Unveiling the role of surface, size, shape and defects of iron oxide nanoparticles for theranostic applications†

Geoffrey Cotin,[a,b] Cristina Blanco-Andujar,[a] Francis Perton,[a] Laura Asín, [c]
Jesus M. de la Fuente, [c] Wilfried Reichardt,[d,e,f] Denise Schaffner,[d]
Dinh-Vu Ngyen,[a] Damien Mertz, [a] Céline Kiefer,[a] Florent Meyer, [g]
Simo Spassov,[h] Ovidiu Ersen, [a] Michael Chatzidakis,[i] Gianluigi A. Botton,[i]
Céline Hénoumont,[j] Sophie Laurent, [j] Jean-Marc Greneche, [k]
Francisco J. Teran, [l,m] Daniel Ortega, [l,n,o] Delphine Felder-Flesch [a] and
Sylvie Begin-Colin ⋆[a,b]

Iron oxide nanoparticles (IONPs) are well-known contrast agents for MRI for a wide range of sizes and shapes. Their use as theranostic agents requires a better understanding of their magnetic hyperthermia properties and also the design of a biocompatible coating ensuring their stealth and a good biodistribution to allow targeting of specific diseases. Here, biocompatible IONPs of two different shapes (spherical and octopod) were designed and tested *in vitro* and *in vivo* to evaluate their abilities as high-end theranostic agents. IONPs featured a dendron coating that was shown to provide anti-fouling properties and a small hydrodynamic size favoring an *in vivo* circulation of the dendronized IONPs. While dendronized nanospheres of about 22 nm size revealed good combined theranostic properties (r_2 = 303 mM s^{-1}, SAR = 395 W g$_{Fe}^{-1}$), octopods with a mean size of 18 nm displayed unprecedented characteristics to simultaneously act as MRI contrast agents and magnetic hyperthermia agents (r_2 = 405 mM s^{-1}, SAR = 950 W g$_{Fe}^{-1}$). The extensive structural and magnetic characterization of the two dendronized IONPs reveals clear shape, surface and defect effects explaining their high performance. The octopods seem to induce unusual surface effects evidenced by different characterization techniques while the nanospheres show high internal defects favoring Néel relaxation for magnetic hyperthermia. The study of octopods with different sizes showed that Néel relaxation dominates at sizes below 20 nm while the Brownian one occurs at higher sizes. *In vitro* experiments demonstrated that the magnetic heating capability of octopods occurs especially at low frequencies. The coupling of a small amount of glucose on dendronized octopods succeeded in internalizing them and showing an effect of MH on tumor growth. All measurements evidenced a particular signature of octopods, which is attributed to higher anisotropy, surface effects and/or magnetic field inhomogeneity induced by tips. This approach aiming at an analysis of the structure−property relationships is important to design efficient theranostic nanoparticles.

[a]*Université de Strasbourg, CNRS, Institut de Physique et Chimie des Matériaux de Strasbourg, UMR 7504, F-67034 Strasbourg, France. E-mail: sylvie.begin@unistra.fr*
[b]*Labex CSC, Fondation IcFRC/Université de Strasbourg, 8 allée Gaspard Monge BP 70028, F-67083 Strasbourg Cedex, France*
[c]*Instituto de Nanociencia y Materiales de Aragón (INMA) CSIC-Universidad de Zaragoza & Centro de Investigación Biomédica en Red de Bioingeniería, Biomateriales y Nanomedicina (CIBER-BBN), 50018 Zaragoza, Spain*
[d]*Department of Radiology, Medical Physics, Medical Center, University of Freiburg, Faculty of Medicine, University of Freiburg, Germany*
[e]*German Cancer Consortium (DKTK), Heidelberg, Germany*
[f]*German Cancer Research Center (DKFZ), Heidelberg, Germany*
[g]*Université de Strasbourg, INSERM, UMR 1121 Biomaterials and Bioengineering, FMTS, F-67000 Strasbourg, France*
[h]*Geophysical Centre of the Royal Meteorological Institute, 1 rue du Centre Physique, 5670 Dourbes, Belgium*

[i]*Dept of Materials Science and Engineering, McMaster University, 1280 Main Street West, Hamilton, Ontario, Canada, L8S 4M1*
[j]*Université de Mons, General, Organic and Biomedical Chemistry Unit, NMR and Molecular Imaging Laboratory, 7000 Mons, Belgium*
[k]*Institut des Molécules et Matériaux du Mans IMMM UMR CNRS 6283, Université du Maine, Avenue Olivier Messiaen, 72085 Le Mans Cedex 9, France*
[l]*iMdea Nanociencia, Campus Universitario de Cantoblanco, 28049 Madrid, Spain*
[m]*Nanobiotecnología (iMdea-Nanociencia), Unidad Asociada al Centro Nacional de Biotecnología (CSIC), 28049 Madrid, Spain*
[n]*Condensed Matter Physics Department, Faculty of Sciences, University of Cádiz, 11510 Puerto Real, Spain*
[o]*Institute of Research and Innovation in Biomedical Sciences of Cádiz (INiBICA), 11009 Cádiz, Spain*
†Electronic supplementary information (ESI) available. See DOI: 10.1039/d1nr03335b

1. Introduction

In the field of the synthesis and functionalization of iron oxide nanoparticles (IONPs) for biomedical applications, most research studies aim at developing multifunctional theranostic NPs that can allow both disease staging and therapy delivering locally. For example, some of these theranostic nanoparticles would allow monitoring therapy by imaging.[1–6] The current challenge in iron oxide-based NP engineering is thus to improve their design to allow the combination of magnetic hyperthermia (MH) therapy and imaging as a contrast agent in the same nano-formulation with the best possible efficiency to reduce the dose injected to the patient.

Superparamagnetic IONPs have already been exploited commercially as T2 contrast agents for MRI[7] and are of particular interest as biodegradable and non-toxic nano-objects compared to other contrast agent (CA) families.[8,9] As a rule of thumb, the higher the saturation magnetization (Ms) value, the better the contrast, although this value depends not only on the NP structure but also on its aggregation state and the ability of water molecules to diffuse through the organic coating close to the magnetic core.[7,8]

IONPs are also being developed for MH.[10,11] When exposed to alternating magnetic fields (AMF) of appropriate intensity and frequency, these NPs release heat locally, to damage cancer cells to a variable extent. The use of MH as a single[12,13] or adjuvant[14] therapy for cancer is closer to wider clinical implementation thanks to the positive results from the seminal clinical trials carried out by MagforceTM (Germany),[7,15–17] a nanomedicine company that succeeded in rolling-out MH therapy across Europe.[18] Nonetheless, there is currently a need for improving the nanomaterials available for MH to, for example, reduce the injected dose, better address difficult tumor locations or lower the frequency and/or intensity of the applied field. Different parameters can be modified to increase the effective heat loss of IONPs such as their size, shape and/or composition, among others. Indeed, the amount of heat generated by IONPs is highly dependent on their structural and magnetic properties. Recent studies have shown that spherical iron oxide NPs with a mean size around 20 nm show suitable features for MH.[8,9] More precisely, for frequencies and magnetic field amplitudes used in MH, prior studies carried out using field conditions where $H \times f < 5 \times 10^9$ Am^{-1} s^{-1} suggested an optimal diameter of 14 nm for standard spherical NPs. However given the variation in anisotropy of "magnetite" ($Fe_{3-x}O_4$) NPs with the same size (but synthesized by different methods), the experimental optimal diameter appears to be in a wide range between 12 and 20 nm.[9,14,19] Indeed, the magnetic properties of IONPs strongly depend on their synthesis method,[20–22] while values of the Specific Adsorption Rate (SAR) depend strongly on the experimental parameters (field frequency and amplitude, viscosity, and NP concentration) but also on others related to experimental limitations.[23]

In addition, the modification of the size of the IONPs is limited because their superparamagnetic behavior disappears beyond a given size, leading to suspensions whose colloidal stability is affected by magnetic interactions. To circumscribe this problem, other options are available to improve the heating capabilities of NPs, for example by modifying their shape or composition. Among the highest SAR values reported for NPs with different shapes, one may cite Guardia et al.[24] who showed that cubic IONPs with a mean size of 19 nm presented tremendous heating power as well as Lartigue et al.[25] who developed nanoflowers consisting of aggregates of nanocrystals sharing common crystallographic planes. High relaxivity and SAR values have also been reported for octopod shaped NPs.[26,27] Alternatively, doping with Mn or Co[14,19,28] has also been found to increase the heating power. Pellegrino et al. boosted the heating power of the cubic NPs by doping them with cobalt.[29] The synthesis of NPs with other shapes was also reported such as nanoplates[30,31] or nanotubes.[32] Indeed, many advances have been made in synthesis methods of NPs, revealing that the thermal decomposition method is one of the most – if not the most – versatile ones to tailor the nanoparticle shape, as exemplified by the so produced nanocubes,[33–35] the spherical NPs with different sizes[36] and also the octopods,[26,27,37] thus produced. However, no clear trend has been established on the parameters that are mainly responsible for theranostic properties.[8]

Another key point is the design of the organic coating,[38] which is also challenging due to the multiple functions that organic coating have to fulfil. Indeed, the molecules anchored to the surface of the NPs can add different functions, such as dyes for optical imaging, targeting ligands to reach the target tissue or cells, or therapeutic agents (drug delivery). Other desirable functions include preventing NPs from agglomeration in a physiological environment and favoring their biodistribution and bioelimination (by preventing opsonization of NPs and increasing their ability to escape the reticulo-endothelial system (RES)). In addition to polymers which have been widely studied until now, another class of molecules is emerging, i.e. small dendrons.[39–42] Bifunctional dendrons are promising because the diversity of functionalization provided by the arborescent structure simultaneously meets the need for biocompatibility, low toxicity, large in vivo stability and specificity. The grafting of dendrons on the surface of 10 nm IONPs using phosphonate groups as a coupling agent has led to a new generation of MRI CAs. These nano-objects show relaxivity values higher than those of commercial CAs combined to a very favorable biodistribution in mice without a significant uptake in healthy tissues and in particular the liver (there is an uptake and then quick clearance).[22,43–45] The use of these dendrons appears as a good way to ensure, after the grafting step, a mean hydrodynamic size below 100 nm together with a narrow size distribution in suspension, both being prerequisites for a good biodistribution, i.e. avoiding RES uptake.

In this work, spherical and octopod-shaped NPs, whose synthesis optimization is detailed in reference,[30] are coated with small dendron molecules and their in vitro and in vivo theranostic properties are studied and correlated with their micro-

structural, surface and magnetic signatures. Their magnetic properties were studied in depth and correlated with their properties as contrast agents for MRI and as heating agents for magnetic hyperthermia.

2. Experimental conditions

Synthesis of the iron stearate precursor

Iron stearate (III) named FeSt$_3$ was prepared by precipitation of sodium stearate and ferric chloride salts in an aqueous solution as previously reported.[30]

Synthesis of spheres

Iron oxide nanospheres (NS) were synthesized by thermal decomposition of an iron stearate precursor in the presence of oleic acid (OA) in an organic solvent. For the synthesis of NPs with a mean size around 20 nm: FeSt$_3$ (1.85 g, 2 mmol) was mixed with OA (1.89 g, 6.7 mmol) in squalane (15.8 g, 19.5 ml) and dibenzylether (DBE, 0.53 g, 0.5 ml) in a two neck RBF. The mixture was heated under stirring to 120 °C and kept at this temperature for 60 min without a reflux condenser in order to dissolve the reactants and remove the water residues. The condenser was then connected to the flask and the solution was heated to 330 °C (5 °C min^{-1}) and kept under reflux for 60 min under air. After cooling to RT, a black and viscous suspension was obtained which was solubilized in chloroform (10 ml). The NPs were precipitated by addition of an excess of acetone and washed three times with chloroform and acetone at a ratio of 1 : 4 at 14 000 rpm for 5 min by centrifugation. The

NPs were resuspended in THF (50 ml) and stored until further use. The so obtained IONPs display a mean size of ~18 nm and are named NS18. A higher reflux temperature of 335 °C led to IONPs with a mean size of 22 nm named NS22.

Synthesis of octopods

Iron oxide nano-octopods (NO) were synthesized from commercial iron stearate (III). FeSt$_3$ (0.735 g, 0.9 mmol) was mixed with OA (1.02 g, 3.6 mmol) in DBE (20 mL) in a two neck-RBF. The mixture was heated at 120 °C under stirring and kept at this temperature for 60 min without a reflux condenser in order to dissolve the reactants and remove the water residues. The condenser was then connected to the flask and the solution was heated to 250 °C (5 °C min^{-1}) and kept at this temperature for 60 min. The solution was then brought to 320 °C (10 °C min^{-1}) and kept at the reflux temperature for 60 min in air. After cooling to RT, a black solution was obtained. The NPs were washed as previously described. The so obtained NO displayed a mean size of 27.8 nm and are named NO28. The size has been tuned by adapting the FeSt$_3$: OA ratio and a ratio of 1 : 3 led to NO with a mean size of 17.2 nm named NO18.

Dendronization of nanoparticles by a direct grafting process

We have already reported the synthesis of dendron molecules.[46–48] The scheme of the dendron D2-2P is presented in Fig. 1. Dendronization consists of a direct grafting process,[48] typically a suspension of 1 mL of NP@OA (NPs with a mean diameter of 10 nm) in THF (5 mg mL^{-1}) was put in contact with 7 mg of dendron molecules in 4 mL of THF. The
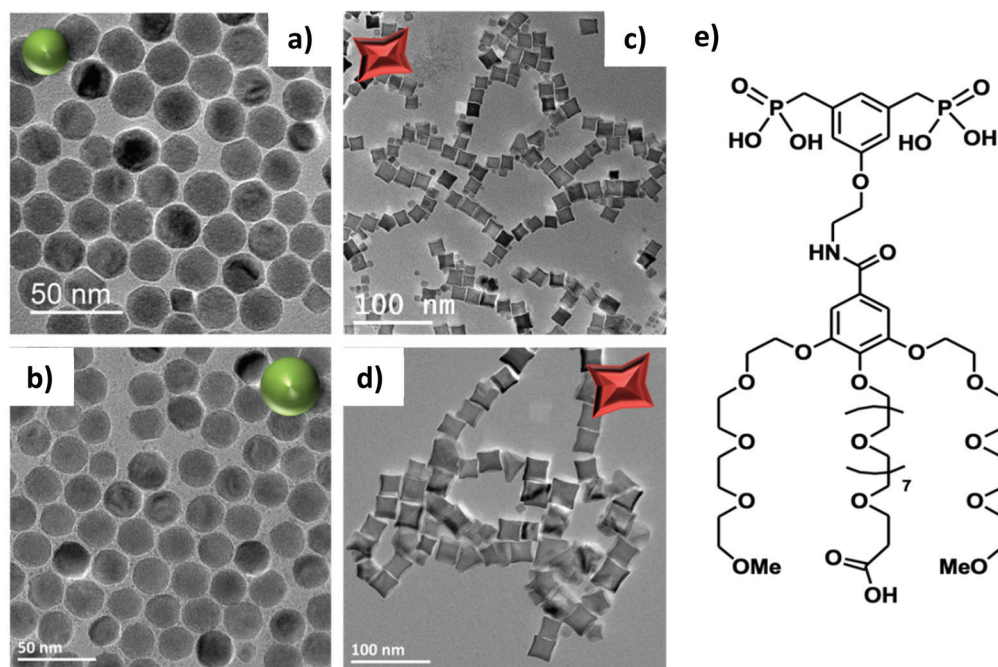

Fig. 1 TEM images of iron oxide NPs with different shapes and sizes: NS18 (mean size 17.2 ± 2 nm) (a), NS22 (mean size 22 ± 2 nm) (b), NO18 (17.2 ± 2.2 nm) (c) and NO28 (27.8± 4 nm) (d) and Scheme of the D2-2P dendron molecule (e).

mixture was magnetically stirred for 24 h. The NPs@dendrons were then precipitated by addition of hexane and centrifugation (8000 rpm, 3 min). The supernatant was discarded and the NPs were easily dispersed in 10 mL DI water.

The standard protocol was further adapted here as due to their higher size, the magnetic interactions are no more negligible and the concentration of NPs was decreased by increasing the volume of the NP solution to 20 ml instead of 1 ml. Then the time was adapted: spheres and octopods were put in contact for 48 h. However, octopods were grafted with a two-step process. After 48 h of dendronization, the solution was purified by ultrafiltration to remove the free oleic acid. After 3 steps of purification, the NPs were put in contact with 7 mg of dendrons for the same time as the first step.

The NPs@dendrons were then precipitated by addition of hexane followed by centrifugation (8000 rpm, 3 min). The supernatant was discarded, and the NPs were easily dispersed in 10 mL DI water. The grafted NPs were then separated from the ungrafted dendron molecules by ultrafiltration. After at least 4 purification steps, the pH of the NP suspensions was adjusted to 7 and the suspensions were ready for characterization.

Glucose coupling

Into 5 mL of a NP solution were added 1 mg Fe per mL, 0.3 mmol (80 mg) of glucose (4-aminophenyl β-D-glucopyranoside) and 78 μmol (15 mg) of EDC ((1-ethyl-3-[3-dimethylaminopropyl]carbodiimide hydrochloride)). After stirring overnight, the NPs were purified by ultrafiltration. After 4 purification steps, the NPs were ready for characterization. The IR spectrum in Fig. S15† confirmed the presence of glucose on dendronized octopods.

Structural characterization techniques

The NPs were characterized by transmission electron microscopy (TEM) with a JEOL 2100 microscope operating at 200 kV (point resolution 0.18 nm). The size distribution of NPs was estimated from the size measurements of more than 300 nanoparticles using ImageJ software. For octopods, the TEM size corresponds to the mean length of the longest axis (nm). Electron Energy Loss Spectroscopy (EELS) measurements were carried out on a FEI Titan 80–300 scanning transmission electron microscope operated at 200 kV and fitted with an electron monochromator and a Gatan quantum energy filter. Data processing of the EELS fine structures to extract the valence state of Fe was carried out using independent component analysis within the Hyperspy open software.

The X-ray diffraction (XRD) pattern was collected at room temperature with a Bruker D8 Advance diffractometer equipped with a monochromatic copper radiation source ($K\alpha$ = 0.154056 nm) and a Lynx-Eye detector in the 25–65° (2θ) range with a scan step of 0.03°. High purity silicon powder (a = 0.543082 nm) was systematically used as an internal standard. Profile matching refinements were performed through the Fullprof program[49] using Le Bail's method[50] with the modified Thompson-Cox-Hasting (TCH) pseudo-Voigt profile function.

Standard infrared spectra were recorded between 4000 and 400 cm^{-1} with a Fourier transform infrared (FTIR) spectrometer, Spectrum 100 from PerkinElmer. Samples were gently ground and diluted in non-absorbent KBr matrixes.

^{57}Fe Mössbauer spectra were recorded at 300 K and 77 K using a conventional constant acceleration transmission spectrometer with a ^{57}Co(Rh) source and a bath cryostat where the sample chamber is under a He atmosphere. In-field spectra were obtained using a cryomagnet where the external magnetic field is oriented parallel to the γ-beam and the sample chamber is under a He atmosphere. The preparation of the Mössbauer samples is discussed below. The zero-field and in-field spectra were fitted by means of the MOSFIT program[51] involving asymmetrical and lines with Lorentzian profiles and an α-Fe foil was used as the calibration sample. The values of the isomer shift are quoted relative to that of α-Fe at 300 K.

Granulometry measurements were performed on a MALVERN (nano ZS) apparatus for each NP suspension and allowed determining a mean hydrodynamic diameter (D_h). The efficiency of ligand exchange was assessed by performing high resolution magic-angle spinning NMR (HR–MAS NMR). HRMAS experiments were carried out on a Bruker FT-NMR Avance 500 equipped with an 11.75 T superconducting ultrashield magnet. All the experiments were performed at a spinning rate of 5 kHz with a 50 μL zirconium rotor.

Magnetic measurements – experimental setting

DC magnetic measurements were carried out on all synthesized magnetic NPs using a Magnetic Property Measurement System Model 3 (MPMS3) from Quantum Design (QD). Before measurements, the MPMS3 was calibrated using the Pd standard reference sample provided by QD. The calibration was carried out at 298 K following the standard QD procedure for the vibrating measurement mode VSM moment calibration. The VSM calibration factor was adjusted in a way that the difference between calibration measurement and the theoretical value was less than 0.1%. The MPMS3 measurements were carried out using the QD powder caps and a brass holder. Prior to measurements, a blank measurement of the empty brass holder was carried out, but it revealed negligible contribution to the magnetic moment of the sample.

Mass determination. Dry residues of NP suspensions were measured instead of liquid state samples. The iron mass per sample was determined by weighing the NP suspensions before drying and considering the previously known iron concentration. The NP suspensions were dried in air at 300 K for about 24 h. The masses were determined with a precision balance from Ohaus (precision 0.01 mg at 0.1 mg, repetition 0.02 mg at 0.1 mg) with internal calibration and compensation for air flow and vibrations. The balance is mounted onto an anti-vibration table.

The empty capsule mass was determined 8 to 11 times, and the NP suspension mass was determined at least 11 times. On average, the mass of the NP suspension was about 26.29 ± 0.18 mg. Next, the NP volume was calculated using the water

density at 25 °C. The previously determined Fe concentrations of the suspensions permitted then calculating the mass of Fe in the dry residue. A direct mass determination of the dry residue was not possible. The measured magnetic moments were then normalized by the mass of Fe in the dry residue.

Magnetization cycles. Four quadrant hysteresis loops were acquired in vibrating measurement mode (VSM) between ±3 T, using a vibration peak amplitude of 6 mm and an averaging time of 2 s. The field was stabilized at each step before measurement; the field driving rate between steps was set to 10 mT s^{-1}. Loops were acquired at various temperatures between 1.8 and 300 K. For some low temperature loops, the sample was cooled in a field of +3 T. Each loop consists of about 190 points per branch, which are logarithmically distributed over the ±3 T range.

AC magnetic measurements were performed under AMF in colloidal dispersions of the synthesized NPs (at iron concentration 1.5 g L^{-1}). AC hysteresis loops were traced at room temperature using a commercial inductive magnetometer (AC Hyster Series; Nanotech Solutions, Spain). Each magnetization curve was repeated three times to obtain an average magnetization curve, subsequently extracting the main parameters of interest (coercivity, remanence, and loop area). In order to accurately quantify the magnetic losses of IONP suspensions, SAR values were calculated according to SAR = $A \times f$,[52] where A is the magnetic area and f is AC magnetic field frequency. The output signals were normalized to the magnetite mass employed in each experiment.

Next, zero-field cooled (ZFC) and field cooled (FC) magnetization experiments were performed with the studied IONPs. Due to the always present residual field of the superconducting magnet, two procedures were tested prior to the experiments to limit this effect. (A) The field was set to zero in oscillating mode after centering the sample in an 800 kA m^{-1} field and (B) repeating step (A) and subsequent application of a small field opposite to the residual field of the magnet. No difference was observed and therefore procedure A was applied prior to ZFC experiments.

The measurements were carried out under the same conditions as the hysteresis loops, *i.e.* VSM mode, 6 mm peak amplitude and 2 s averaging time. A rate of 5 K min^{-1} was chosen for all cooling and warming curves. The magnetic moment was measured continuously during warming and cooling (scanning mode). Data acquisition started after ZFC and 20 min waiting time at 3 K. ZFC/FC measurements were generally acquired in 3 different fields: 5, 10 and 16 kA m^{-1}. Only the curves of sample NC were acquired in different 18 fields from 0.16 to 400 kA m^{-1}.

Magnetic measurements – data processing

Hysteresis. The measured data were corrected for the residual field of the superconducting magnet. In short, a correction function C(H) was calculated from hysteresis measurements of the Pd standard reference sample. C(H) was then subtracted from the hysteresis measurements of the samples. Also, the high-field slope, caused by dia- or paramagnetic con-

tributions, was determined following the approach to saturation method.[53] This consists of fitting the high-field data between 800 and 2400 kA m^{-1} resp. −800 and −2400 kA m^{-1} with the function $a - bHp + cH$, with $p = 1$ in the present case. The procedure was applied to all four hysteresis quadrants. Only quadrants with $R2 > 0.9$ (regarding the fit of the data) were taken to calculate the average high-field susceptibility. Finally, a mean high-field correction was subtracted from the hysteresis data. Saturation magnetization σ_s, saturation remanence σ_{rs} and coercive fields at $\sigma = 0$ were obtained from the interpolated, corrected hysteresis data by root finding.

ZFC/FC experiments. ZFC and FC curves consist of about 1800 data points and were filtered with a simple moving average filter with a length of 21 points. The filtered ZFC and FC curves were interpolated linearly to obtain an analytical expression. The derivative of the difference −[FC(T)–ZFC(T)] was calculated and then digitized. This resulted in a dataset consisting of about 2600 points, which was filtered also with a simple moving average filter of length 21. For data interpretation, the −[FC(T)–ZFC(T)] *vs.* T curve was used for interpretation.

Calorimetry measurements. The heat dissipation of NP suspensions was evaluated with a DM1 system (nB Nanoscale Biomagnetics, Spain) operating in a frequency range of f = 395–795 kHz and a field amplitude of H = 4–16 kA m^{-1}. 1 ml samples were first thermalized for 10 min at 20 °C in the apparatus. Field and frequency were then applied for 5 min. The generated temperature profiles were fitted to the Box Lucas model[54] using the built-in software (nB Nanoscale Biomagnetics, Spain). It allowed determining $[dT/dt]_{t=0}$ and then calculating the SAR value by using the following equation:

$$\text{SAR} = m_s \times C_s / m_{Fe} \times [dT/dt]t = 0$$

where m_s and C_s are respectively the mass (kg) and the heat capacity (J kg^{-1} K^{-1}) of the sample, m_{Fe} (g) is the mass of iron element present in the sample and $(dT/dt)_{t=0}$ is the derivative function of the temperature at $t = 0$ (K s^{-1}).

Biocompatibility evaluation

Cell culture. Human hepatocarcinoma Huh7 cells were propagated in Dulbecco's modified Eagle's medium supplemented with 10% of decomplemented fetal bovine serum (FBS), 0.5% penicillin and 0.5% non-essential amino acids.

MTT assay. The number of viable cells after dendronized NP exposure was evaluated by the MTT (3-[4,5-methylthiazol-2-yl]-2,5-diphenyl-tetrazolium bromide) assay. In brief, Huh7 cells (1.104 cells per well) were seeded in a 96-well plate and kept overnight for attachment. The next day, the medium was replaced with fresh medium with various concentrations of dendronized NPs diluted in complete culture medium and cells were allowed to grow for 24 h. After completion of incubation, the medium was discarded and well thoroughly washed with 200 μL of PBS in order to eliminate all remaining extracellular nanoparticles. 200 μL of cell culture medium + MTT (0.5 mg mL^{-1}) is added to each well and cells are incu-

bated for further 3 h 30 at 37 °C and 5% CO_2. After completing the incubation, medium is carefully discarded and 100 μL of DMSO was added to each well and incubated for 15 min at room temperature under orbital shaking. Color developed after the reaction was measured at 550 nm using a Xenius microplate reader (SAFAS, Monaco). Cell viability was obtained as the ratio of mean absorbance of triplicate readings of sample wells (Asample) compared to the mean absorbance of control wells (sample Acontrol). DMSO was used as the negative control, ADMSO as shown in the following equation.

$$\text{Cell viability} = \frac{A_{\text{sample}} - A_{\text{DMSO}}}{A_{\text{control}} - A_{\text{DMSO}}} \times 100\%$$

MRI experiments

Relaxivity measurements, T_1 and T_2 relaxation time measurements, of dendronized IONPs were performed on a Bruker Minispec 60 (Ettlingen, Germany) working at a Larmor frequency of 60 MHz (1.41 T) at 37 °C. The longitudinal (r_1) and transverse (r_2) relaxivity values were obtained according to the general equation of relaxivity $R = R_0 + r \times [\text{CA}]$, where [CA] is the concentration of the contrast agent (CA) (*i.e.*) the concentration of Fe in IONPs, R is the relaxation rate ($1/T$) in the presence of the CA, R_0 is the relaxation rate of the aqueous medium in the absence of the CA and r is the relaxivity value of the CA.

Nuclear magnetic resonance dispersion (NMRD) profiles. Proton NMRD profiles were recorded using a Stelar Fast Field Cycling relaxometer (Mede, Italy). The system operates over a range of magnetic fields extending from 0.25 mT to 0.94 T (0.01–40 MHz) at 37 °C. T_1 and T_2 measurements were performed on a Bruker Minispec mq60 (Karlsruhe, Germany) working at a Larmor frequency of 60 MHz (1.41 T) at 37 °C.

MRI biodistribution experiments

The MR biodistribution experiments were performed in the MMTV-PyMT (mouse mammary tumor virus-polyoma middle tumor-antigen) mouse model of breast cancer. All animals had free access to food and water and were exposed to standardized conditions. Before the measurements, the animals were allowed to acclimatize to the ambient conditions for at least 1 week. A total of 4 female mice were used.

Anesthesia was initiated in an animal induction chamber using a mixture of 2% isoflurane (Forene, AbbVie, Wiesbaden, Germany) and 98% oxygen. It was maintained with an animal nose mask applied with a mixture of 1.5% isoflurane (Forene) and 98.5% oxygen at a flow rate of 0.6 l min^{-1}. During the measurement, the body temperature of the animals was kept stable at 37 °C with a hot water bath system. The electrocardiogram (ECG) and respiration (spontaneous breathing) were continuously monitored to control the general state of the animals.

The MR scans were conducted using a preclinical 9.4 Tesla scanner (BioSpec 94/21, Bruker, Ettlingen, Germany) and a dedicated mouse quadrature coil with an inner diameter of 38 mm (Bruker, Ettlingen, Germany).

The applied MR scanning protocol consisted of a localizer and a T_2-weighted spin echo RARE (Rapid Acquisition with Relaxation Enhancement) sequence. This sequence was used for anatomical reference and to detect susceptibility artefacts causing signal voids induced by the NPs. The RARE sequence featured a FOV of 30 × 35 mm^2 and a matrix size of 256 × 300 mm^2. The slice thickness is 1 mm with no slice spacing to achieve contiguous image sets of the whole volume (TR/TEeff/FA: 2000 ms/17 ms/180°, echo train length: 4). For the evaluation of the NP uptake in the liver, tumor and brain, a multi spin-multi echo (MSME) T2-map was obtained to quantify T2 effects using the same geometry as the T2-RARE sequence, echo time and echo spacing of 8 ms and altogether 10 echo images.

After an initial baseline measurement, a water solution of NPs was injected intravenously into the tail vein of the animals using a self-made catheter (PE-10 tubing, 100 cm length). 2 mice were injected octopods NO28 coated with dendron molecules and 2 mice were injected glucose-coupled octopods. The injected volume was adapted for each mouse to standardize the iron load to 2.5 mg Fe per kg body weight. The catheter was flushed by injecting 100 μl of sodium chloride (0.9%). Subsequently, post-injection scans were performed at time point 30 min, 2 h, 24 h, and 48 h.

All animal experiments were performed in compliance with the German animal protection law, adhering to the standards of good animal practice as defined by the Federation of Laboratory Science Associations (http://www.felasa.eu) and the National animal welfare body GV-SOLAS (http://www.gv-solas.de). Studies were undertaken after the approval of the local authorities and the "Animal Experiment Commission Freiburg" ("Tierversuchskommission Regierungspräsidium Freiburg") with the animal experiment permission number G-19/162.

In vitro and in vivo magnetic hyperthermia

In vitro Huh-7 cells were seeded on a 10 mm cover glass and transferred into a 48-well plate at a concentration of 10^5 cell per well. Cells were incubated for 24 h with Dulbecco's modified Eagle's medium supplemented with 10% of decomplemented fetal bovine serum (FBS), 0,5% penicillin and 0,5% non-essential amino acids (37 °C in 5% CO_2) and then supplemented with a NP suspension (4 mM Fe, 2 ml, complete media) for 24 h at 37 °C in 5% CO_2. Cells were then thoroughly rinsed with 2 mL of cold PBS.

In order to achieve a homogeneous exposure of the cell monolayer to the AC field using the DM1 system (nB Nanoscale Biomagnetics, Spain), a bespoke sample holder was designed to accommodate a 10 mm cover slide in a reservoir of complete media. The holder was designed to fit into the environmental chamber designed by nB nanoscale biomagnetics (nB Nanoscale Biomagnetics, Spain). The cell monolayer was transferred into the bespoken sample holder and supplemented with complete medium containing 25 mM HEPES. The sample chamber positioned the cell monolayer at the point of maximum field amplitude of the DM1 system. Cells were then exposed for 1 h to AMF at a magnetic field ampli-

tude of 11.9–27.9 kA m^{-1} at a frequency of 252–796 kHz. Cells were then returned to culture and imaged at different time points with the aid of an apoptotic/necrotic/healthy cell detection kit (PromoKine). Fluorescence images were captured using a Nikon Elipse TE200 with 63× PL APO (1.4 NA) objective equipped with a Nikon Digital Camera (DS-Q11MC with NIS-Elements software) and processed with ImageJ (http://rsb.info.nih.gov/ij/).

In vivo **magnetic hyperthermia.** Female 6-week C57BL/6 mice were commercially obtained (Charles River) and after a week of acclimation 2.5×10^5 EL6 cells in 100 μL cell culture medium were injected subcutaneously into the right flank with a 25G needle. After 7 days, tumors were small but big enough to inject NPs intratumorally. 70 μL of a sterile (passed through a 0.2 μm filter) 2.6 ± 0.2 mg Fe per mL (in PBS) MNP solution were injected intratumorally per mice (about 182 μg Fe per tumor) with a 30G needle. NP injection was performed in one point of the tumor. The same day of NP injection and the following two days mice were exposed to an alternating magnetic field (AMF) using a commercial device from NanoScale Biomagnetics company (DM3 model). Each AMF application consisted of 30 min exposure time at 105 kHz and 18 kA m^{-2}. Mice were anesthetized with isoflurane and were maintained during the AMF exposure onto a hot water bath system that prevents the mice to suffer hypothermia. Rectal temperature was registered during the AMF exposure to monitor the general state of the animals.

Tumor dimensions (length, width and height) were daily measured with a caliper and also the mouse weight was recorded. Tumor growth was calculated as (tumor volume)/(initial tumor volume). After the last AMF exposure, mice were maintained for 3 days or until tumors started to ulcerate.

Mice were euthanized by CO_2 inhalation and blood was directly extracted from the heart. The tumor was removed and fixed in 4% PFA and processed to perform Hematoxylin/Eosin and Blue Perls staining.

MH experiments were performed with NPs coupled with glucose. Similar *in vivo* MH experiments were performed with NPs coupled with glucose. Trying to observe the antitumoral effect at longer post-treatment times in human derived cancer cell lines some experimental details were modified. Male 6-week nude mice were commercially obtained and after a week of acclimation 2×10^6 HCT-116 (human colorectal cancer cell line) cells in 100 μL DMEM were injected subcutaneously into the left flank with a 25G needle. After 12 days, 100 μL of a sterile 2 mg Fe per mL (in PBS) NP solution were injected intratumorally per mice (200 μg Fe per tumor) with a 30G needle. Besides, AMF conditions were also tuned for using higher frequency and amplitude but maintaining the H_0f value below the biological safety limit (196 kHz and 26 kA m^{-1}). The rest of the conditions of the AMF application and post-treatment evaluation were the same as the previous *in vivo* experimental approach. The experiment is described in Scheme 1.

All animal procedures were performed in accordance with the RD53/2013 law and the Guidelines for Care and Use of Laboratory Animals of Aragon Biomedical Research Centre (CIBA). Experimental procedures were approved by the Animal Ethics Committee of the University of Zaragoza.

Results and discussion

Structural characterization of iron oxide NPs of different sizes and shapes

IONPs with spherical (NS) and octopod (NO) morphologies and with different mean sizes were synthesized through the thermal decomposition process.[30,55] Nanospheres were synthesized in order to highlight the effect of shape anisotropy and because diameter around 20 nm has been reported optimal for MH.[9] NS and NO of different sizes have also been synthesized to study the potential effect of size. TEM images of the spheres (NS18 and NS22) and octopods (NO18 and NO28) are illustrated in Fig. 1. The structural characterization performed on NS22 and NO28 samples by IR spectroscopy (Fig. S1 and S2†) and XRD (Fig. S2†) is representative of results obtained with all NS and NO. They showed that all the synthesized NPs present a spinel structure close to the magnetite $Fe_{3-x}O_4$ composition. The lattice parameter and crystallite sizes have been determined from the profile matching refinement of the XRD pattern (Fig. S2†).

Scheme 1 Experimental setup for *in vivo* magnetic hyperthermia.

Nanospheres (lattice parameter for NS22: 8.391 Å) would have a composition close to that of magnetite (8.396 nm, JCPDS file 19-629). However, their crystallite size is smaller than the mean size determined in TEM images (crystallite size of 13 nm when the TEM mean size is 22 nm). This is often related to the presence of defects inside the NS volume. Indeed, the nuclei formed during the thermal decomposition process have a wüstite $Fe_{1-x}O$ composition and thus the magnetite composition of NS results from oxidation of the wüstite phase during the synthesis process.[56] The oxidation of $Fe_{1-x}O$ has been reported to generate defects such as dislocation or antiphase boundaries[30,47,57] and this has also been demonstrated recently by Pellegrino *et al.*[58] In Fig. 2, the presence of defects has been evidenced by performing a FFT treatment of the HRTEM image. Such defects would also be responsible for the observed lattice parameter very close to the magnetite ones.[59] The investigation of the oxidation of $Fe_{1-x}O@Fe_{3-x}O_4$ nanocubes detailed in ref[59,60] showed that stress is generated at the core–shell interface and within the spinel shell due to the epitaxial growth and oxidation mechanisms of the wüstite phase. A higher lattice parameter than that of the stoichiometric magnetite was noticed and attributed to the presence of these defects induced by the oxidation. To check that the composition of NS was really the magnetite one, IR spectroscopy and Mössbauer spectrometry were used as they are among the most suitable techniques to discriminate between magnetite and maghemite phases. The Mössbauer study is detailed below and shows that the composition is not pure magnetite (~40% of stoichiometric magnetite (Table 1)). The Fe–O bands

in IR spectra (Fig. S1 and S2†), displaying a main band at 580 cm^{-1} with a shoulder towards larger wavelengths, are characteristic of an oxidized magnetite phase confirming again that the composition of the iron oxide phase cannot be ascertained only from the XRD pattern.

For NO, the composition is closer to that of maghemite (8.346 Å, JCPDS file 39-1346) from consideration of the lattice parameter: 8.364 and 8.370 Å for NO18 and NO28 respectively. This was confirmed by Mössbauer spectrometry (Table 1) and consideration of the Fe–O bands in IR spectra (Fig. S1 and S2†). The largest crystallite sizes were measured along directions <400> and <511> for NO28 and <220> and <440> for NO18. A crystallite size of 25 nm is calculated along <400> and of 23 nm along <511> for NO28 and of 15 nm along <220> and 15 nm along <440> for NO18. The fact that the crystallite size relies on a specific crystallographic direction is in favor of a stronger anisotropy for this shape with different shape factors. Investigations of defects by HRTEM (Fig. S3†) and inverse FFT showed the presence of few defects in octopods in agreement with their more oxidizing synthesis conditions (presence of polar solvents) by comparison with nanospheres.

Structural and magnetic characterization of dendronized IONPs

Structural characterization. NPs have been then coated with dendron molecules by a direct ligand exchange process consisting in introducing dendron molecules into a THF suspension of NPs coated with oleic acid.[46–48] The ligand exchange/dendronization was confirmed by infrared spectroscopy (Fig. S1†) and HR-MAS measurements (Fig. S4†) which showed a very limited amount of remaining oleic acid. The amount of remaining oleic acid was shown previously very important to avoid unspecific uptake of dendronized NPs by cells or *in vivo*.[61] The effect of this dendronization step on the IONP composition and properties has been then investigated. ^{57}Fe Mössbauer spectrometry was used to discriminate the different Fe species and to determine their respective oxidation states from the isomer shift values. Mössbauer spectra were retrieved from all dendronized NPs, but some experiments were also performed on oleic acid coated NPs for comparison. It is important to emphasize that the following Mössbauer spectra were recorded on samples containing very small quantities (2–5 mg) of powders after focusing with a lead mask to obtain an efficient surface containing about 5 mg Fe per cm^2. The Mössbauer spectra of all dendronized NPs at 300 K and 77 K look *a priori* quite similar as all of them exhibit magnetic sextets in addition to a small quadrupolar feature at the center

Fig. 2 Defects in NS22 NPs (zone axis [110]): (a) HRTEM NS22 image and (b) fast Fourier transform (FFT) image obtained from the analysis depicted by the red square. (c) Inverse of the FFT obtained by selecting the {220} family plan showing the presence of defects.

Table 1 Mean values of hyperfine parameters refined from Mössbauer spectra recorded at 77 K on NPs with different shapes (IS: isomer shift, B_{hf}: hyperfine field, stoichiometry "3 − x" in $Fe_{3-x}O_4$, <e> thickness of the maghemite shell, <t> thickness of the canted layer for tetrahedral and octahedral sites)

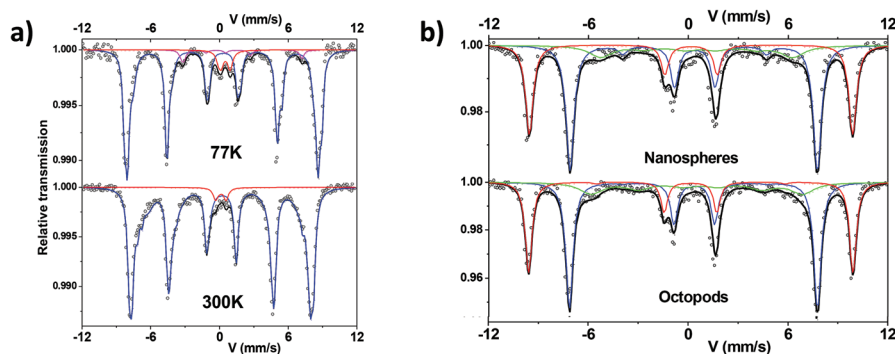|	<IS> mm s^{-1} ±0.01	<B_{hf}> T ±0.5	γ-Fe_2O_3 (%) ±3	Fe_3O_4 (%) ±3	<Stoichiometry> ±0.02	<e>$_{\gamma\text{-}Fe_2O_3}$ nm ±0.5	<t> nm ±0.5
NS22	0.52	50.5	60	40	2.80	2.9	0–0.5
NO18	0.48	51.4	79	21	2.74	2.5	0.1–0.1

Fig. 3 (a) Representative 300 K and 77 K Mössbauer spectra of sample NS22 (blue: sextet, red: doublet, pink: quadrupolar component) and (b) Mössbauer spectra of samples NS22 and NO18 under an applied field of 8 T at 12 K.

(Fig. 3 and S5†). At 300 K, the lines exhibit some asymmetrical broadening resulting from intrinsic electronic properties but due to the NP size, a superparamagnetic doublet should be observed at 300 K. Magnetic measurements presented below confirmed a superparamagnetic behavior of our NPs. In fact, we are in the particular case where NPs with relaxation times between 140 ns (measurement time of Mössbauer spectrometry) and 1 s (measurement time for a single point of a hysteresis curve) would be seen as non-superparamagnetic in the Mössbauer spectra, but as superparamagnetic in hysteresis loops. From relaxivity measurements in Table 3, the relaxation times deduced from this range roughly between 0.002 and 0.2 s, which is much larger than the characteristic observation time of Mössbauer spectroscopy and below the observation time of the hysteresis measurements.

Thus, the magnetic component was described by means of several magnetic sextets with different isomer shift values. They range from 0.3 up to 0.45 mm s^{-1}, attributed to Fe ions with different oxidation states between Fe^{3+} and about $Fe^{2.7+}$. This confirms a composition corresponding to an oxidized magnetite. One first way is to estimate the mean stoichiometry of each set of NPs. Those results can be also modeled in terms of a core–shell model which consists of stoichiometric magnetite and maghemite phases, as previously described in refs. 20,62; the proportions allow the thickness of the maghemite shell to be estimated, dependent on the mean morphology of NPs. Table 1 summarizes the mean values of hyperfine parameters corresponding to NPs after dendronization. In addition, the central part is better described by adding a quadrupolar component assigned to (high spin) HS Fe^{3+} species. At this stage, this small component could be attributed to the presence of Fe species connected to dendrons, originating some local Fe environments close to those of iron phosphate compounds. At 77 K, the spectra are composed of lines, which are narrower than those observed at 300 K. Different fitting procedures were considered to describe those spectra. The spectrum characteristic of octopods exhibits some broadening of the internal wings of the outer lines which must be described by means of several magnetic sextets with different isomer shift values. Consequently, the octopods consist of a non-homogeneous phase, the stoichiometry of which should vary continuously from magnetite at the center and maghemite at the surface. In the case of the nanospheres, one observes some shoulder in the internal wing of the 2nd and 6th magnetic lines. This feature can be likely assigned to a blocked HS Fe^{2+} species, which confirms again that the nuclei of NPs consist of wüstite,[56] which oxidizes leading to a magnetite-maghemite core–shell structure with defects.

Mössbauer spectra have also been recorded under an applied field of 8 T at 12 K on both samples and are compared in Fig. 3b. Using such instrumental conditions, the magnetic sextets are well split into two main magnetic sextets, which can be unambiguously attributed to tetrahedral and octahedral Fe sites, according to the ferrimagnetic structure. Their resolution leads to accurate estimation of the proportions of tetrahedrally and octahedrally-coordinated Fe^{3+} species; for both investigated samples, the ratio tetra : octa is found rather close to 1 : 2. In addition, the corresponding isomer shift values are also suitably consistent with those observed at 77 K and 300 K. However, a better refinement is obtained by means of a third magnetic component to describe the internal wings of magnetic lines: the larger value of the isomer shift suggests the presence of Fe species with valency states intermediate between 2 and 3, in perfect agreement with zero-field results as mentioned above. The last information is about the intensity of intermediate lines, which is related to the canting of magnetic moments with respect to the external magnetic field. The canting appears usually lower for Fe^{3+} species located in tetrahedral sites (<10°) than those in octahedral sites (10–20°) while that of the third component exceeds 30°. This later value is consistent with a noncolinear magnetic structure in the bulk originated from the magnetic frustration resulting from the combined effects of the cationic topology correlated to the local stoichiometry and the magnetic anisotropy of Fe^{2+}. In the case of NS, the thickness of the canted layer is estimated at about 0.5 nm for the octahedral sites and close to zero for tetrahedral ones, suggesting that the surface results preferentially from octahedral units. The global magnetic structure remains rather similar in the case of octopods, with a larger canting, which can be due to the morphology.

NS and NO were further probed by TEM-EELS analyses. With the NS22 NPs, the EELS analysis performed for several NPs showed that the Fe valence is almost the same in the core of NPs and at their surface. Two typical spectra obtained by separating the EELS signals corresponding preferentially to the two core and surface regions are shown in Fig. S6.† While the energy position of the peak did not change, there appeared to be a slight broadening of the Fe L23 edge. This effect could be due to the presence of Fe linked to the dendron molecules.

The EELS analysis performed for NO28 (Fig. 4) showed that the core of NO contained a larger relative amount of Fe^{3+} atoms compared to that of Fe^{2+}, while the surface has more Fe^{2+} components (Fig. 4). This allowed us to conclude that for all the analyzed NPs the surface layer would have a lower valence than the core one. The inhomogeneous distribution of the Fe^{2+} and Fe^{3+} components through the particle could be the result of either the presence of a very localized $Fe_{1-x}O$ phase or a mixed oxide with reduced valence. It should be mentioned here that, as the spectra acquired at this edge are relatively noisy, it is difficult to properly determine an eventual change in the spectral shape through the particle. This analysis would confirm Mössbauer results that the composition of octopods is inhomogeneous and evidences a surface effect.

Both TEM-EELS analysis and Mössbauer spectroscopy support that the composition of octopods is rather different (inhomogeneous) from that of isotropic NPs and that the surface of octopods is rather different from that of isotropic spherical NPs.

Magnetic characterization. The ZFC/FC curves (Fig. S7†) of all NPs are characteristic of superparamagnetic-like NPs with an average blocking temperature located at the surroundings of the maximum T_{max} of the ZFC curve. The corresponding temperature derivatives of the ZFC curves (Fig. 5 and S7†) allowed identifying the most distinct peaks whose values are given in Table 2 featured by each sample. This analysis is important to confirm the structural characterization previously presented, since all the iron oxide phases involved present unique magnetic features that can be detected through a careful appraisal of ZFC/FC curves. Likewise, the evolution of magnetization with temperature is essential to identify other relevant aspects of the nanoparticle magnetism that directly affects the total anisotropy energy of the different samples.

The broad intense peak P1 (Fig. 5 and Table 2) showed a marked field dependence, which means that it corresponds to the blocking process of most of the NPs within the sample but not all of them due to the size distribution always present to a variable extent. P1 shifts towards lower temperatures as the field increases because the probing field decreases the anisotropy barrier the NPs have to overcome during their unblocking process. Consequently, the population of unblocked NPs at the lower end of the temperature range increases for higher applied fields. Therefore, this peak can be assimilated to the average blocking temperature of NPs.

The presence of a P2 peak, attributed to the Néel temperature (T_N) of $Fe_{1-x}O$, has been checked but no P2 peak has been evidenced in all samples.

Peak P3 does not show a field dependence, although it becomes more intense for higher applied fields. It corresponds to the Verwey transition of magnetite (T_V), and it is confirmed by the small bump in the FC branch at the same temperature (Fig. S7†). Although this transition is expected to occur at higher temperatures in the bulk phase, it has been reported
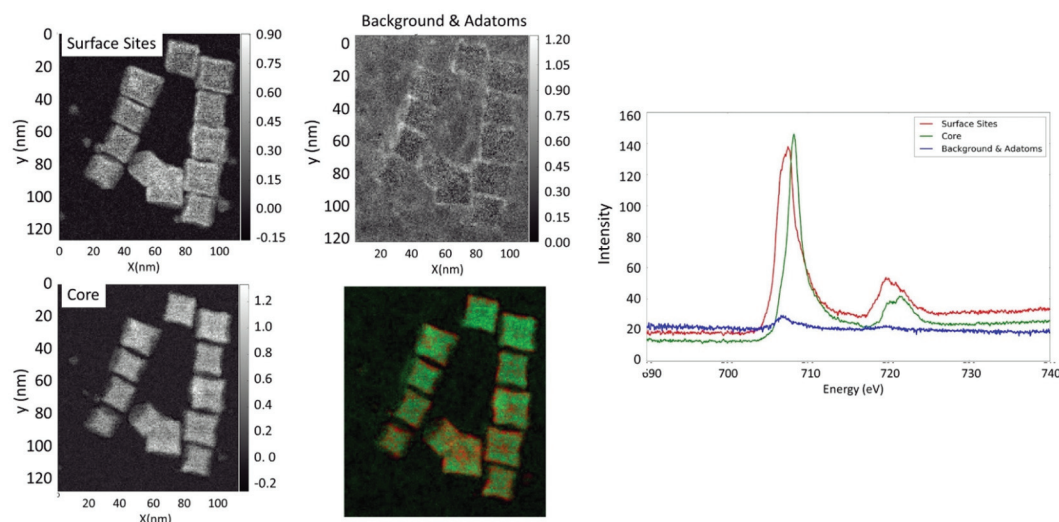

Fig. 4 EELS analysis of several NO28 NPs: HAADF image along with the decomposition of the Fe L23 edge EELS signals in their different contributions as extracted *via* independent component analysis. The individual maps show the spatial distribution of the surface, core and background signals (left panel) with the corresponding spectra (right) of the surface layer (red spectrum), core (green spectrum) and the background and adatoms (blue spectrum). The left panel shows the respective spatial maps of the separated components with the color coded map showing the superposed overlapping images of these separate contributions (surface components (red), core components (green) and background with ad-atoms on the support film (blue)).

Fig. 5 Differential ZFC magnetization curves with respect to the temperature for samples (a) NO18 and (b) NS18 obtained at external fields of 4, 8 and 16 kA m^{-1}.

Table 2 Assignment of the peaks observed in the differential ZFC/FC curves in Fig. 5 with indication of the corresponding temperature values in Kelvin

Peak #	Field (kA m^{-1})	Sample		Assignment
		NS18	NO18	
P1	4	180	225	T_{max}
	8	162	193	
	16	156	128	
P3	4	90	90[a]	T_V
P4	4	20	20	T_f

[a] Very weak; only at the highest applied field.

that it shifts towards lower temperatures for smaller particle sizes,[63] similarly to the experimental observations for the Morin transition in hematite nanoparticles,[64] which even disappears for sufficiently small NPs.[65] Other explanations are also a deviation from stoichiometry of the magnetite phase: T_V has been reported to be very sensitive to the stoichiometry, because the Fe vacancy increase in the $Fe_{3-x}O_4$ leads to a decrease in the strength of the Fe–Fe exchange on B sites. Indeed, T_V is reported to decrease from $Fe_{2.995}O_4$ at 125 K to $Fe_{2.934}O_4$ at 100 K.[20] The progressive intensity increase of P3 is merely incidental, and stems from the shift of P1 at increasing fields (Fig. 5). As mentioned, the Verwey transition is usually seen as an abrupt jump in both ZFC and FC magnetization, which is observed in NS22 and NO28 (Fig. S7b and d†). This is in agreement with the fact that the higher is the NP mean size, the higher is the magnetite amount.[66] With sample NO18, we only see a modest peak that is suggested to be due to a lower content of magnetite in the NPs as confirmed by the above

structural characterization (they are oxidized into maghemite to a sizeable extent).

Peak P4 does not depend on the applied field, and given the low temperature at which it appears, it is ascribed to the spin-glass-like behavior of the superficial spins, more precisely to their freezing temperature (T_f). The field is not able to contribute to their blocking process, and only very low temperatures can freeze them and block their magnetic moments. One may notice that this peak is clearly more visible for NO18 and NO28 and suggested a higher canting degree on the surface spins compared to NS samples. It would confirm TEM EELS and Mössbauer results on a more complex surface state of octopods.

The magnetization (($\sigma(H)$) curves at room temperature of all NPs are characteristic of a superparamagnetic regime (Fig. S8†)—*i.e.*, zero coercivity and remanence—, while a ferrimagnetic behavior appears at 5 K as expected for NPs below their blocking temperature. To evaluate the occurrence of exchange interactions between the core of NPs and a canted layer of spins at the surface[36] field-cooled magnetization curves FC (($\sigma(H)$) have been further recorded, and an exchange field H_{bias} characteristic of such exchange has been determined (Fig. S8†). The methodology has been described elsewhere.[67] The general trend of H_{bias} with temperature (Fig. S9†) is a small and positive exponential decay towards higher temperatures in all samples. In the inset of the FC hysteresis loop at 5 K of NS22, the so-called "wasp-waisted" behavior can be observed (Fig. S8d,† inset). This effect has been traditionally associated with the coexistence of multiple phases although it has been also proposed that it may well be due to the apparition of two switching fields in a single phase sample.[68] Such duality would stem from the combination of interparticle

interactions (for example due to a concentration increase) with easy-plane anisotropy, which correspond to a negative first anisotropy constant, as opposed to the uniaxial anisotropy (positive first anisotropy constant) typically considered in systems of single-domain and superparamagnetic NPs. The subtle wasp-waisted hysteresis effect on the sample is also compatible with the existence of a residual multi-domain fraction. These results are in agreement with the structural characterization, since we have shown from XRD measurement that the coherence length was smaller than the TEM size. Thus, the exchange bias observed here may be due to a surface and volume spin canting.[36]

The temperature dependence of H_C (Fig. S10†) is qualitatively similar to that found by other authors in other nanoparticle systems[69] and subsequent theoretical calculations,[70] and it fits to a radial surface anisotropy model quite well. This form of anisotropy is added to the uniaxial anisotropy induced by the inner spins of each NP, and its value is mainly determined by the exchange coupling between both types of spins —inner and superficial ones— and by the angle formed between the applied field and the easy anisotropy axis. H_C shows a rather monotonic increase with decreasing temperatures for values up to ≈100 K. From this point onwards, H_C increases at a much faster rate as the spin freezing temperature of the superficial spins approaches around 20 K, as revealed by the corresponding ZFC curves in Fig. S7† almost doubling its value within the last 50 K. Nevertheless, from T = 20 K, H_C does not increase noticeably, which coincides with the temperature where all the spins—including the superficial ones—are assumed to be fully exchanged and also aligned with the external field. Additionally, since $H_c \propto K/\sigma_s$, and both K and σ_s are intrinsic properties given by the crystalline structure of the material, the observed deviations may in principle be ascribed to structural changes or finite-size effects that may affect both K and σ_s. H_c values reveal that sample NO18 shows the lowest coercivity change from 300 K down to 5 K. Given the dependence of H_C on the particle volume, this fact indicates that this sample has the lowest population of blocked NPs, or in other words, most of their constituent NPs are already unblocked at room temperature. NO18 presents a lower H_C than NS22.

To better evaluate the heating mechanism and if it is related either to Néel and/or Brownian relaxation, magnetization curves have been recorded at 100 kHz and also in media with different viscosity (Fig. 6 and S11†).[71,72] AC hysteresis loops at 100 kHz showed very distinctive features depending on the sample size and shape. Nano-octopods present the largest opening of the AC hysteresis loops. Indeed, the area of the curves showed that the magnetic losses of nanospheres improve upon increasing particle size, whereas the octopod shape shows a remarkably larger area than NSs under similar AMF conditions, in agreement with the calorimetric SAR values. The opening of the loops reveals further qualitative information related to the magnetic anisotropy. The loops from sample NO28 are not as well pronounced as the other samples under similar AMF
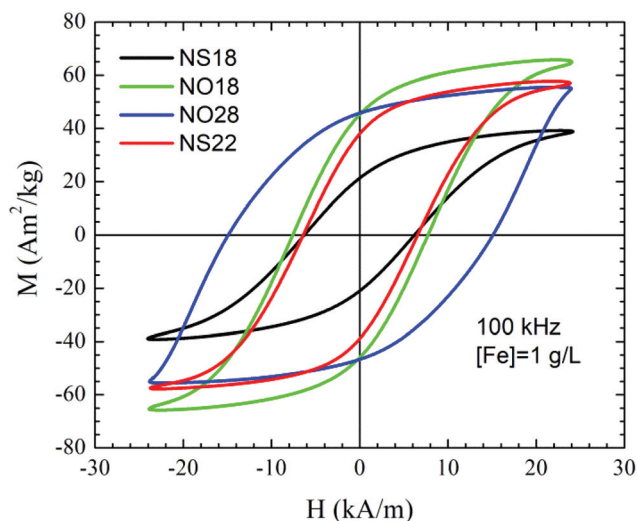

Fig. 6 AC hysteresis loops obtained at 100 kHz and 24 kA m^{-1} for water dispersions of samples NS18, NS22, NO18, and NO28 at a NP concentration of 1 g$_{Fe}$ l^{-1}.

conditions. Sample NO28 has a wide elliptical shape whose coercive field is close to the maximum external field intensity. Such AC hysteresis loops are typically characterized by minor loops due to large magnetic anisotropy values.[71] Large anisotropy values also influence the prevalent magnetic relaxation processes[71] and reference therein. Thus, Brownian relaxation typically dominates for larger anisotropies or NP sizes. The relevant contribution of the Brownian process into the effective magnetic relaxation mechanism can be clearly evidenced when the viscosity of the medium is varied (Fig. S11†). Thus, our results suggest that the Brownian relaxation is the main contribution to the heating mechanism for NO28, whereas Néel relaxation prevails for the other samples.

In vitro investigations with dendronized IONPs

The colloidal stability of NPs in different physiological media has been assessed with DLS measurements (Fig. S12†). The mean hydrodynamic size of all dendronized NPs is below 60 nm (Table 3).

Then relaxivity and SAR measurements were performed on the dendronized NP suspensions. The main properties are summarized in Table 3 and in Fig. S13, 14.† A good T_2 contrast agent is expected to display both a high r_2 value and a high r_2/r_1 ratio.[8] NS22 displays higher relaxivity values as well as SAR values by comparison with NS18 as expected with such isotropic NPs whose Ms increases with the NP size.[36,73] By contrast, NO18 show higher r_2 and SAR values than NO28. All dendronized NPs can be used as MRI contrast agents.

From SAR values, both nanospheres and octopods exhibit high performance for MH. As expected, and shown in Fig. S13† for NO18 and NS18, SAR values increase when frequency and/or magnetic field amplitude increase. Heat losses were observed at all tested frequencies and magnetic fields for

Table 3 Main MRI and magnetic heating properties of the different shaped NPs in water suspension (D_h is the mean hydrodynamic size). SAR value for NO18 at 1 g $^{-1}$ may not be accurate as evaporation occurred due to the elevated temperature but as shown in Fig. S13,† the SAR values remain the highest even at lower AMF

IONPs	TEM size (nm)	D_h (nm)	Relativities (in mM^{-1} s^{-1}) at 1124.75 kA m^{-1}			Specific absorption rate (SAR) ± 20 (W g$_{Fe}$$^{-1}$) f = 796 kHz and H = 16 kA m^{-1}	
			r_1	r_2	r_2/r_1	C = 1 g L^{-1} Fe	C = 0.5 g L^{-1}
NS10[74]	10	18	13	78	6	No heating	No heating
Resovist	3–5	62	9.7	189	19.5	—	—
Endorem	ND	120–130	10	141	14	—	—
NS22	22.2 ± 1.8	28	10	303	30	395	425
NS18	17.9	35	12	189	16	300	350
NO18	17.2	51	17	405	24	950	1000
NO28	26.1 ± 4	60	8	274	34	528	ND

octopods, whereas no significant heat loss was measured for spherical NPs at 4 kA m^{-1}.

As the amount of *in vivo* internalized NPs may be low after intravenous injection, the effect of NP concentration on SAR values has been investigated (Fig. S14†) and evidenced that even at low concentration, octopods present high heating values. The heating performance of NS18 is also preserved at quite low concentration. As can be seen from these data, octopods show the best properties in terms of relaxivity and SAR values even at low concentration (Fig. S14†) regardless of the particle size.

The determination of the NMRD profile of a contrast agent consists of measuring the r_1 relaxivity at different magnetic fields. Obtained by a fast field cycling method, it allows a fast analysis of the properties of a contrast agent and determines in which frequency range/magnetic field, it will be most effective. NMRD profiles were recorded for all NPs and are represented in Fig. 7. NS10 presents the typical profiles expected for superparamagnetic NPs. NS22, NO18 and NO28 present a different behavior from the classical ones expected for superparamagnetic NPs. The bump/maximum observed around 1–3 MHz for classical NPs is not observed. The position of this bump is dependent on the size of the NPs. The profile of the NS22 can thus be explained by their size (22 nm) and the formation of some chains under the applied magnetic field in agreement with the spontaneous alignment in chains observed when the NS are deposited on TEM grids (Fig. S15†) and during NP deposition experiments on substrates.[75] Such anisotropy would further explain their high relaxivity and SAR values (Table 3).

Both NO profiles present high relaxivities at low field. This is not explained by the NMRD theory, which was developed for symmetrical systems.[76] Since anisotropy energy controls the NP behavior at low field, the observed high relaxivity values may be explained by the fact that NO displays a high anisotropy energy (see the anisotropy calculations reported in the ESI†). Unfortunately, no theoretical model was developed for such kind of structures to date. Furthermore, octopods may also align (Fig. S15†) during the measurements increasing thus their anisotropy, but another hypothesis could be that their peculiar shape with elongated corners induces local magnetic field heterogeneities which affect positively relaxivity values. These profiles evidenced thus a high anisotropy in these systems especially for octopods. This would explain the high relaxivity and SAR values observed for octopods by comparison with nanospheres: there is a contribution of the shape anisotropy and anisotropy induced by their alignment under AMF.

Due to their excellent performance in magnetic hyperthermia and imaging, the octopod-shaped NPs have been selected for further *in vivo* investigations.

In vivo MRI and cellular and *in vivo* MH with dendronized octopods

In vivo MRI. Biodistribution of octopods NO28 coated with dendron molecules was investigated over 48 hours (Fig. 8). NO28 were selected due to their higher hydrodynamic size and since they were used for MH experiments also. The contrast change in the liver implies a high NP uptake within the first 2 hours post-injection. Later on, the contrast change was no longer present, indicating that the NPs were eliminated within
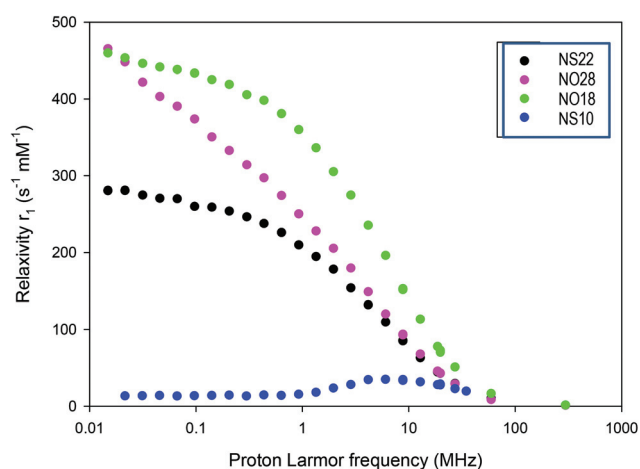

Fig. 7 NMRD profiles of the different NPs (NS10 corresponds to iron oxide NPs with a mean diameter of 10 nm and dendronized).
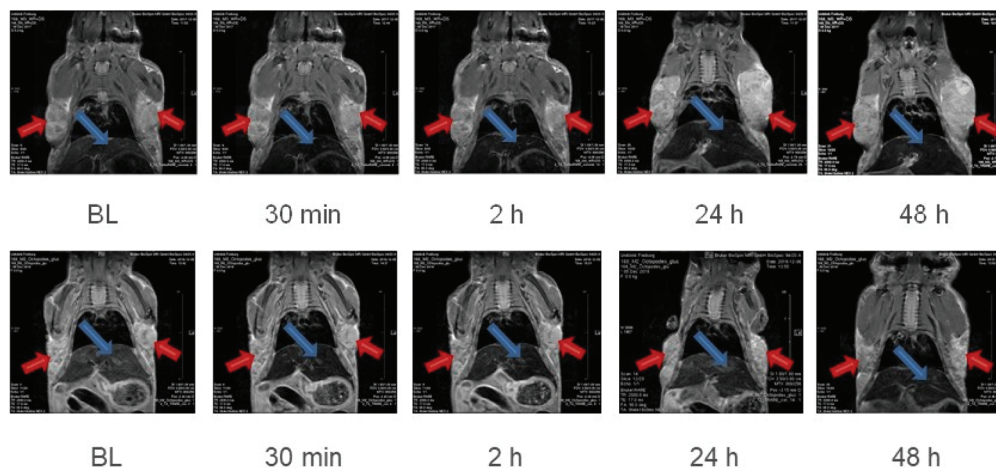
Fig. 8 Biodistribution of dendronized octopods NO28 at different time points over 48 h post-injection. Upper row: without glucose coating. Lower row: with glucose coating. The tumors are pointed out with red arrows and the liver with a blue arrow.

the period of 2–24 hours post-injection. In contrast, in the tumor and brain, no contrast change was visible, suggesting that no NP uptake took place in these tissues (brain images not shown). In the tumor and brain, the MSME-T_2-map showed no significant changes in T_2 times for the different time points (data not shown). In the liver, T_2 times could not be reliably quantified due to the low signal. These results confirmed what we have already observed with 10 nm sized spherical NPs coated with dendron molecules,[61] that dendronized NPs displayed nonspecific uptake. The dendron coating conferred to NPs even with bigger sizes such as antifouling properties.

To try to enhance the tumor internalization, glucose was coupled to dendronized octopods (Fig. S16†). By attaching glucose on the surface of NPs, no enhanced NP uptake into the tumor tissue was observed (Fig. 8). The amount of coupled glucose needs to be tuned to ensure a NP internalization in tumors visible by MRI. Indeed, only a very low amount of glucose was grafted as an aggregation due to hydrogen interaction or the loss of charge with high density of glucose was observed.

Cell internalization studies and *in vitro* magnetic hyperthermia with octopods. Cytotoxicity tests demonstrated no toxicity in all NPs up to 8 mM (Fig. S17†). TEM images of cells after incubation with NPs at different concentrations (2 and 4 mM) were obtained and the results are shown in Fig. 9.

The population of NPs inside phagosomes is low at both tested concentrations. In addition, some local organization has been observed depending on the shape. NS22 tended to form rings, whereas NO18 preferred to align. The results altogether demonstrated a weak internalization, which is attributed to dendron molecules preventing NPs from nonspecific internalization.

In vitro magnetic hyperthermia was carried out with NO18 octopods. Cell monolayers loaded with NO18 (4 mM) were exposed to the corresponding AC field for 1 h and then

Fig. 9 TEM images of NPs internalized by cells as a function of the concentration. Insets present a zoom of NPs inside the cells.

returned to culture to study the time-dependent response to the treatment. Control experiments without magnetic NPs can be found in Fig. S18.† Field amplitude and frequency conditions were chosen to mimic the settings used for SAR evaluation. Two conditions were selected, with relatively high frequency/low field and low frequency/high field combinations, but a very similar $H \times f$ factor (even if it is slightly higher than the $H \times f$ factor recommended for clinical trials: 5×10^9 Am^{-1} s^{-1} (ref. 77)).

When cells were exposed to 395 kHz and 27.8 kA m^{-1} for 1 h, no significant cell death was observed just after the MH treatment at $t = 0$ (no effect of possible Eddy currents) and only a marginal increase was seen 6 h after the MH treatment (Fig. 10). A similar trend was observed when cells were exposed to 795 kHz and 11.9 kA m^{-1} for 1 h. However, cell death was significantly increased at 24 h after MH treatment (Fig. 10).
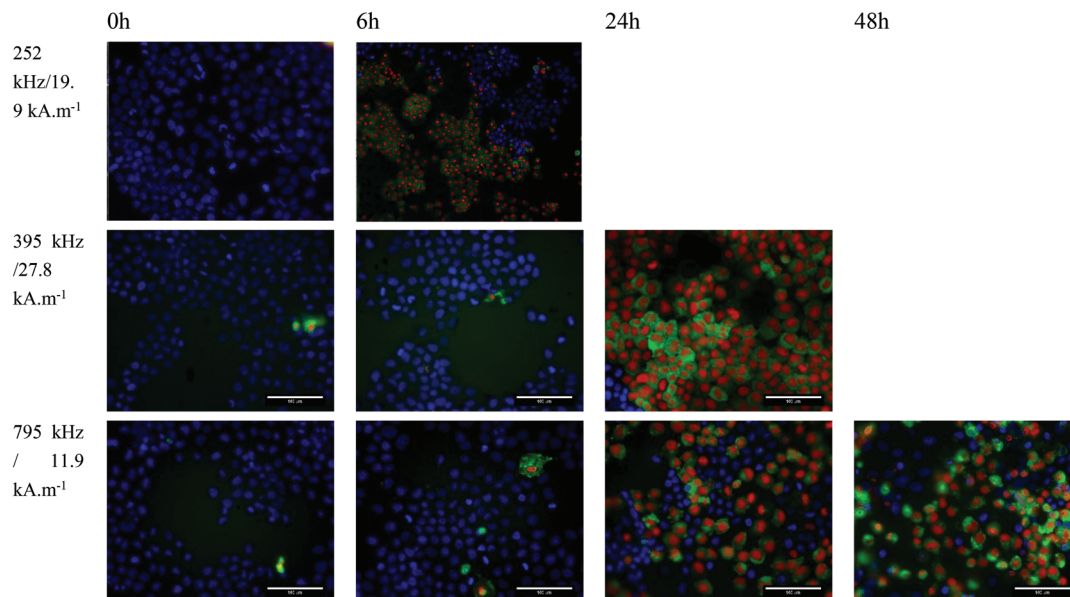
Fig. 10 Huh-7 cells loaded with 4 mM NO18 exposed to (i) 252 kHz and 19.9 kA m^{-1} at t = 0 h and 6 h after 1 h treatment; (ii) 395 kHz and 27.8 kA m^{-1} at t = 0 h, 6 h and 24 h after 1 h treatment and (iii) 795 kHz and 11.9 kA m^{-1} at t = 0 h, 6 h, 24 h and 48 h after 1 h treatment. Cells were labeled with Annexin V-FITC (green), PI (red) and hoechst (blue).

Even though the difference in the $H \times f$ factor was very small, cell death was significantly higher when a lower frequency and higher magnetic field amplitude (395 kHz and 27.8 kA m^{-1}) were used. A quantitative evaluation of the cell response is very difficult as cells quickly formed aggregates and floaters upon cell death, yielding unreliable cell counting. Nevertheless, despite a low NP internalisation, a cell death reaching *ca.* 50% was estimated in that case, whereas 20–30% was observed under a higher frequency.

Based on the observed results at lower frequency, a third experiment series was carried out at a more reduced frequency. When cells were exposed to 252 kHz and 19.9 kA m^{-1} for 1 h, a rapid uneven response was observed (Fig. 10). Rapid formation of cell aggregates and floaters was observed in some areas, whereas other cells were completely unaffected. At 6 h, more than *ca.* 60% of the cells were labelled as dead forming big aggregates and detaching. It was not possible to image at 24 h as all cells were dead floating. These *in vitro* experiments confirmed the good magnetic heating properties of octopods for MH especially at low frequency.

In vivo magnetic hyperthermia. To further check the *in vivo* magnetic hyperthermia properties of dendronized octopods, NO28 were injected intratumorally into mice. These preliminary experiments detailed in the ESI (Fig. S19a†) showed no effects in tumor inhibition growth. PERLS staining performed in order to detect NO28 in tissue sections (Fig. S19b and c†) evidenced that NPs are mainly in the extracellular matrix, even if some can be detected in the tumor. NO28 NPs were very stable and easy to inject, but the main problem is that they stayed in the extracellular matrix instead of being internalized in the tumor. This would confirm again that dendron coating prevents NPs from unspecific internalisation.[61,74]

Fig. 11 Tumor growth rate with NO28 NPs coupled with small amount of glucose without (blue color) and with (red color) magnetic field exposure. Normalization was made against the volume of the tumor the day 1. Day 1 corresponds to the first day of treatment when the injection of the INPs and the first MH application was carried out. Days 2 and 3 animals received MH treatment repetition.

In order to evidence an *in vivo* hyperthermia effect of octopods, further experiments have been performed by coupling glucose at the surface of dendronized NPs (by using the carboxylate function of dendrons) to improve their internalization in tumoral cells. The results given in Fig. 11 show that the coupling of a small amount of glucose succeeded in showing an effect of MH on the tumor growth.

Discussion

NS and NO with different mean sizes[30,55] but with mean sizes promising for observing MH effects have been synthesized and

coated with dendron molecules. Cell internalization experiments with dendronized NS and NO and *in vivo* experiments centered on dendronized NO have confirmed again the antifouling properties ensured by the dendron coating. The dendron efficiency is thus demonstrated whatever the size and shape of NPs and the dendron coating provides high colloidal stability, high relaxivity values (water diffusion around the magnetic core) and biocompatibility. Nevertheless, this performance needs a strong master of the functionalization step which should ensure a quite full ligand exchange with hydrophobic surfactants. Yet, oleic acid (OA) can change the interaction with the cell surface and elicit passive membrane translocation by direct interaction of OA with the fatty acids compounds of the extracellular membrane: this has been attributed to the higher disrupting nature of the kinked chain of these fatty acids that would result in higher magnitude of lipid disruption thus leading to increased cellular uptake,[78] and references therein. But, we recently showed that a dendritic biphosphonic tweezer anchoring at the surface of NPs drastically lowers the amount of OA remaining at the NP surface after the ligand exchange process.[61] Furthermore previously reported studies showed that endocytosis is the main mechanism of cellular internalization of magnetic NPs.[79] Yet, dendritic phosphonates strongly stabilize magnetic NPs through electro-steric interactions, thus preventing the formation of aggregates[48,80,81] Thus, by preventing the aggregate formation, but also by reducing the amount of OA surfactant present on the NP surface, a dendritic coating through a biphosphonic acid allows extremely effective reduction of unspecific cellular uptake, as already shown in various cancer cell lines.[61]

NS display interesting relaxivities and SAR values when their size is larger than 18 nm. Dendronized NO18 were the NPs, which exhibited the highest promise for combining therapy by MH (even at low magnetic field amplitude) and as a contrast agent for MRI. This was confirmed by MH on cells, which evidenced also a particular higher effect at low frequency. The biodistribution investigation by MRI demonstrated again the antifouling properties provided by the dendron coating which is needed to couple glucose on dendronized octopods to be able to observe an effect of MH on tumor growth.

To better understand what are the main characteristics of NO and NS, which can explain the higher properties of NO, the structural and magnetic properties of the different NPs have been investigated by different techniques. XRD and IR spectroscopy characterization techniques showed that all shaped NPs consist of oxidized magnetite before dendronization. After the dendronization step of NPs, Mössbauer data and earlier studies allowed reporting that the core of the NS consists of magnetite covered by maghemite, while octopod-shaped ones probably result from a rather continuous distribution of oxidation states ranging from ferric to intermediate ferric-ferrous-state. TEM-EELS analysis showed that the surface of octopods would contain some lower valence state iron cations. In-field Mössbauer spectrometry showed that for NS, only iron moments in octahedral sites are canted and on a

very small thickness in agreement with earlier studies.[36] By contrast, the canting in NO affects iron on both sites and on a larger thickness. Possible explanation to the particular surface composition of NO could be this canting or the growth process of such anisotropic shape, which may be due to the growth of a $Fe_{1-x}O$ phase which oxidizes or a phosphonatation during the dendronization which occurs differently from that observed usually with isotropic shapes. Indeed phosphate iron II phases exist such as iron II phosphate ($Fe_3(PO_4)_2$) and iron II dihydrogen phosphate $Fe(H_2PO_4)_2$ and a different anchoring of phosphonate from dendron at the surface of such complex surface would be possible. Another possible explanation would be a surface reduction induced by the decomposition of dibenzyl ether, which occurs in such a high temperature range.[56,82]

The comparison of relaxivities and SAR values demonstrated that NS combine also very good MRI and MH properties which increase with their diameter when the opposite is observed with octopods with the smallest size exhibiting the highest performance. The correlation observed between H_C and SAR values in Table S1† confirmed the recent suggestion made by Starsich *et al.*,[83] which states that coercivity values determine the heating capabilities of NPs. More specifically, samples showing lower coercivity values or larger saturation magnetization σ_S to H_C ratios also present a better heating efficiency. In fact, the best 'heater' of the series is sample NO18, which shows the lowest H_C.

The case of NS is quite simple as we have already demonstrated that the composition gets closer to the magnetite one with the increase of their size as well as their saturation magnetization. All the characterization performed here after the dendronisation step confirmed this evolution and especially the more intense peak corresponding to the Verwey transition in ZFC/FC curves for NS22 by comparison with NS18. The dependency of relaxivity and SAR values with size could be easily explained by the enhanced magnetic properties with the size increase (and the observation by Smolensky *et al.*[84]). However, the Néel mechanism is identified as the main heating mechanism when normally in this range of sizes, the Brownian motion should highly contribute.[8] We explain such behavior by the presence of volume defects inside NS. These defects were evidenced by crystallite size measurements from the XRD pattern and HRTEM and confirmed by the high coercive field of the NPs despite their isotropic shape. This is in agreement with recent results of Pellegrino *et al.*[58] who have investigated the MH properties of core–shell wustite@spinel nanocubes at different oxidation steps. Thus, the presence of defects does not affect their magnetic hyperthermia properties and even contribute to them by favoring the Néel relaxation.

Octopods exhibited the highest performances for MRI and MH (in particular at low frequency) clearly related to their shape anisotropy. It has already been demonstrated that relaxivity values can be optimized by varying the NP shape.[84–86] This was observed by Joshi *et al.*[86] and Smolensky *et al.*[84] when they compared spherical and faceted NPs, leading in both cases to higher values of relaxivity for faceted NPs. Similarly, cubic spinel IONPs ($r_2 = 761$ mM^{-1} s^{-1} at 3 T),[87] as well as

octopod IONPs (edge length of 30 nm) (r_2 = 679.3 ± 30 mM^{-1} s^{-1} at 7 T), exhibited significant transverse relaxivity values.[27,29] The high relaxivity values measured in octopod NPs are due to the modified symmetry of the stray field gradients around their elongated edges, causing a change in the diffusion of surrounding water protons. The extent of the stray field gradient dictates the degree of phase coherence loss of protons – the larger r_2 values – when circulating close to the octopods.

Surface effects are also evidenced, such as spin canting and a degree of iron oxidation that varies according to the faces (EELS studies). Nevertheless, this effect seems to depend on the size with a stronger effect for small octopods (relaxivity and SAR measurements). The P4 peak in Fig. 5 corresponding to the surface spin glass is very intense for NO18 by comparison to NO28. The concave faces along elongated corners at the nanoscale make that several iron planes are exhibited at the surface, which is confirmed by the spin canting with spheres only observed in Oh sites when both iron sites are canted with octopods. This complex surface should affect their whole magnetic properties, but the octopods performance is mainly related to their shape anisotropy which should induce locally heterogeneous magnetic field suitable for MRI and MH. Zhou et al.[88] reported that magnetic field inhomogeneity induced by clustering or shape of NPs are favorable to enhance T_2 relaxivity.

The heating of IONPs depends on the total anisotropy: we explain the anisotropy enhancement effect supported by theoretical calculations (see ESI†). The calculated shape anisotropy values for octopods (see ESI†) support the proposed role of the nanoparticle shape in increasing the anisotropy field and hence the effective field "felt" by the NPs. Such shape anisotropy was also evidenced when comparing nanocubes and nanospheres.[89–92] The theoretical total anisotropy values obtained by considering both shape and surface effects on octopod nanoparticles amount to 78.7 kJ m^{-3}, in the same order of magnitude but much higher than that of bulk magnetite (−13.5 kJ m^{-3}).[93] This is translated in a more intense modification of the diffusion of water molecules around NPs. The NO18 sample showed a higher T2 value than NO28. Considering a similar shape anisotropy contribution of the two samples, it is reasonable to ascribe this difference to a more important tip (elongated corner) effect for NO18 than for NO28. Indeed the tip/corner represents a larger part of the volume for NO18 and may introduce a higher local magnetic heterogeneity favorable for enhancing the relaxivity.[88] These tip effects on the magnetic field inhomogeneity explain the unusual NMRD profile and TEM-EELS results.

The AC hysteresis analysis reveals that the bigger octopods NO28 may present a performance reduction in vitro and in vivo due to the prevalent Brownian heating mechanism. The higher viscosity of bodily fluids and tissues will affect the mechanical contribution from the Brownian relaxation to the magnetomechanical torque behind nanoparticle heating processes. The rest of the samples are much less prone to be affected by the medium viscosity and hence their performance should remain unaltered in biological media.

Conclusion

NS and NO were synthesized from own produced precursors and coated with dendron molecules displaying an arborescent architecture. The small size and design of the dendron with two phosphonate groups as anchoring groups at the surface of NPs and with three PEG chains at the periphery have been shown again efficient, through in vitro and in vivo experiments, to ensure antifouling properties to NPs whatever their size and shape. The design of the dendron allowed to improve the ligand exchange process and to limit the amount of remaining oleic acid which favors cell internalization.

The NPs were characterized by different techniques such as in-field Mössbauer spectrometry, HRTEM EELS, determination of NMRD profiles. It was shown that NO and NS exhibit large relaxivity and heating values. The sizeable area enclosed in the measured AC hysteresis loops reflect their good heat dissipation capacity, which is suitable for MH, revealing Néel relaxation as the main heating mechanism, which is the most favorable one when NPs are internalized in cells. The exceptional properties of octopods were further studied by some in vitro and in vivo experiments. The different characterization evidenced their complex surface state and composition due to their concave shape with elongated corners but also a clear shape anisotropy favorable for MRI and MH. Their shape with tip effects induces a magnetic field inhomogeneity, which may also explain the unusual NMRD profile and TEM-EELS results. MH in vitro experiments with NO with mean size around 20 nm evidenced that they were particularly efficient at low frequency.

The observed relationships between structure and properties led to conclude that NS with mean size higher than 20 nm and containing defects that preserve the Néel relaxation for MH, as well as NO with mean size around 20 nm to avoid Brownian relaxation are promising nano-objects for theranostics.

Conflicts of interest

There are no conflicts to declare.

Acknowledgements

References

1 M. Liong, J. Lu, M. Kovochich, T. Xia, S. G. Ruehm, A. E. Nel, F. Tamanoi and J. I. Zink, *ACS Nano*, 2008, **2**, 889–896.

2 J. Kim, Y. Piao and T. Hyeon, *Chem. Soc. Rev.*, 2009, **38**, 372–390.

3 M. De, P. S. Ghosh and V. M. Rotello, *Adv. Mater.*, 2008, **20**, 4225–4241.

4 S. Mornet, S. Vasseur, F. Grasset and E. Duguet, *J. Mater. Chem.*, 2004, **14**, 2161–2175.

5 D. Yoo, J.-H. Lee, T.-H. Shin and J. Cheon, *Acc. Chem. Res.*, 2011, **44**, 863–874.

6 C. Fang and M. Zhang, *J. Mater. Chem.*, 2009, **19**, 6258–6266.

7 S. Laurent, D. Forge, M. Port, A. Roch, C. Robic, L. Vander Elst and R. N. Muller, *Chem. Rev.*, 2008, **108**, 2064–2110.

8 C. Blanco-Andujar, A. Walter, G. Cotin, C. Bordeianu, D. Mertz, D. Felder-Flesch and S. Begin-Colin, *Nanomedicine*, 2016, **11**, 1889–1910.

9 F. Gazeau, M. Lévy and C. Wilhelm, *Nanomedicine*, 2008, **3**, 831–844.

10 I. Rubia-Rodríguez, A. Santana-Otero, S. Spassov, E. Tombácz, C. Johansson, P. De La Presa, F. J. Teran, M. del Puerto Morales, S. Veintemillas-Verdaguer, N. T. K. Thanh, M. O. Besenhard, C. Wilhelm, F. Gazeau, Q. Harmer, E. Mayes, B. B. Manshian, S. J. Soenen, Y. Gu, Á. Millán, E. K. Efthimiadou, J. Gaudet, P. Goodwill, J. Mansfield, U. Steinhoff, J. Wells, F. Wiekhorst and D. Ortega, *Materials*, 2021, **14**, 706.

11 E. A. Périgo, G. Hemery, O. Sandre, D. Ortega, E. Garaio, F. Plazaola and F. J. Teran, *Appl. Phys. Rev.*, 2015, **2**, 041302.

12 K. Maier-Hauff, R. Rothe, R. Scholz, U. Gneveckow, P. Wust, B. Thiesen, A. Feussner, A. von Deimling, N. Waldoefner, R. Felix and A. Jordan, *J. Neuro-Oncol.*, 2007, **81**, 53–60.

13 K. Maier-Hauff, F. Ulrich, D. Nestler, H. Niehoff, P. Wust, B. Thiesen, H. Orawa, V. Budach and A. Jordan, *J. Neuro-Oncol.*, 2011, **103**, 317–324.

14 J. Kolosnjaj-Tabi, R. Di Corato, L. Lartigue, I. Marangon, P. Guardia, A. K. A. Silva, N. Luciani, O. Clément, P. Flaud, J. V. Singh, P. Decuzzi, T. Pellegrino, C. Wilhelm and F. Gazeau, *ACS Nano*, 2014, **8**, 4268–4283.

15 K. Maier-Hauff, R. Rothe, R. Scholz, U. Gneveckow, P. Wust, B. Thiesen, A. Feussner, A. von Deimling, N. Waldoefner, R. Felix and A. Jordan, *J. Neurooncol.*, 2007, **81**, 53–60.

16 K. Maier-Hauff, F. Ulrich, D. Nestler, H. Niehoff, P. Wust, B. Thiesen, H. Orawa, V. Budach and A. Jordan, *J. Neurooncol.*, 2011, **103**, 317–324.

17 http://www.magforce.de/en/home.html.

18 Germany, http://www.eib.org/infocentre/press/releases/all/2017/2017-221-investment-plan-for-europe-eib-backs-german-cancer-therapy-developer-magforce-with-up-to-eur-35m.htm (accessed February 21, 2019).

19 A. E. Deatsch and B. A. Evans, *J. Magn. Magn. Mater.*, 2014, **354**, 163–172.

20 T. J. Daou, G. Pourroy, S. Bégin-Colin, J. M. Grenèche, C. Ulhaq-Bouillet, P. Legaré, P. Bernhardt, C. Leuvrey and G. Rogez, *Chem. Mater.*, 2006, **18**, 4399–4404.

21 J. Santoyo Salazar, L. Perez, O. de Abril, L. Truong Phuoc, D. Ihiawakrim, M. Vazquez, J.-M. Greneche, S. Begin-Colin and G. Pourroy, *Chem. Mater.*, 2011, **23**, 1379–1386.

22 B. Basly, G. Popa, S. Fleutot, B. P. Pichon, A. Garofalo, C. Ghobril, C. Billotey, A. Berniard, P. Bonazza, H. Martinez, D. Felder-Flesch and S. Begin-Colin, *Dalton Trans.*, 2013, **42**, 2146–2157.

23 J. Wells, D. Ortega, U. Steinhoff, S. Dutz, E. Garaio, O. Sandre, E. Natividad, M. M. Cruz, F. Brero, P. Southern, Q. A. Pankhurst, S. Spassov and The RADIOMAG consortium, *Int. J. Hyperthermia*, 2021, **38**, 447–460.

24 P. Guardia, R. Di Corato, L. Lartigue, C. Wilhelm, A. Espinosa, M. Garcia-Hernandez, F. Gazeau, L. Manna and T. Pellegrino, *ACS Nano*, 2012, **6**, 3080–3091.

25 L. Lartigue, P. Hugounenq, D. Alloyeau, S. P. Clarke, M. Lévy, J.-C. Bacri, R. Bazzi, D. F. Brougham, C. Wilhelm and F. Gazeau, *ACS Nano*, 2012, 121129155806007.

26 Z. Nemati, J. Alonso, L. M. Martinez, H. Khurshid, E. Garaio, J. A. Garcia, M. H. Phan and H. Srikanth, *J. Phys. Chem. C*, 2016, **120**, 8370–8379.

27 Z. Zhao, Z. Zhou, J. Bao, Z. Wang, J. Hu, X. Chi, K. Ni, R. Wang, X. Chen, Z. Chen and J. Gao, *Nat. Commun.*, 2013, **4**, 2266.

28 C. S. S. R. Kumar and F. Mohammad, *Adv. Drug Delivery Rev.*, 2011, **63**, 789–808.

29 A. Sathya, P. Guardia, R. Brescia, N. Silvestri, G. Pugliese, S. Nitti, L. Manna and T. Pellegrino, *Chem. Mater.*, 2016, **28**, 1769–1780.

30 G. Cotin, C. Kiefer, F. Perton, D. Ihiawakrim, C. Blanco-Andujar, S. Moldovan, C. Lefevre, O. Ersen, B. Pichon, D. Mertz and S. Bégin-Colin, *Nanomaterials*, 2018, **8**, 881.

31 S. Palchoudhury, Y. Xu, A. Rushdi, R. A. Holler and Y. Bao, *Chem. Commun.*, 2012, **48**, 10499.

32 S. Palchoudhury, W. An, Y. Xu, Y. Qin, Z. Zhang, N. Chopra, R. A. Holler, C. H. Turner and Y. Bao, *Nano Lett.*, 2011, **11**, 1141–1146.

33 M. V. Kovalenko, M. I. Bodnarchuk, R. T. Lechner, G. Hesser, F. Schäffler and W. Heiss, *J. Am. Chem. Soc.*, 2007, **129**, 6352–6353.

34 A. Shavel, B. Rodríguez-González, J. Pacifico, M. Spasova, M. Farle and L. M. Liz-Marzán, *Chem. Mater.*, 2009, **21**, 1326–1332.

35 S. Noh, W. Na, J. Jang, J.-H. Lee, E. J. Lee, S. H. Moon, Y. Lim, J.-S. Shin and J. Cheon, *Nano Lett.*, 2012, **12**, 3716–3721.

36 W. Baaziz, B. P. Pichon, S. Fleutot, Y. Liu, C. Lefevre, J.-M. Greneche, M. Toumi, T. Mhiri and S. Bégin-Colin, *J. Phys. Chem. C*, 2014, **118**, 3795–3810.

37 Z. Zhou, Z. Zhao, H. Zhang, Z. Wang, X. Chen, R. Wang, Z. Chen and J. Gao, *ACS Nano*, 2014, **8**, 7976–7985.

38 N. T. Thanh, *Magnetic Nanoparticles: From Fabrication to Clinical Applications*, CRC Press, Boca Raton, FL, 2012.

39 O. Rolland, C.-O. Turrin, A.-M. Caminade and J.-P. Majoral, *New J. Chem.*, 2009, **33**, 1809–1824.

40 M. J. Cloninger, *Curr. Opin. Chem. Biol.*, 2002, **6**, 742–748.

41 S.-E. Stiriba, H. Frey and R. Haag, *Angew. Chem., Int. Ed.*, 2002, **41**, 1329–1334.

42 R. Duncan and L. Izzo, *Adv. Drug Delivery Rev.*, 2005, **57**, 2215–2237.

43 C. Ghobril, G. Popa, A. Parat, C. Billotey, J. Taleb, P. Bonazza, S. Begin-Colin and D. Felder-Flesch, *Chem. Commun.*, 2013, **49**, 9158–9160.

44 B. Basly, D. Felder-Flesch, P. Perriat, C. Billotey, J. Taleb, G. Pourroy and S. Begin-Colin, *Chem. Commun.*, 2010, **46**, 985–987.

45 G. Lamanna, M. Kueny-Stotz, H. Mamlouk-Chaouachi, C. Ghobril, B. Basly, A. Bertin, I. Miladi, C. Billotey, G. Pourroy, S. Begin-Colin and D. Felder-Flesch, *Biomaterials*, 2011, **32**, 8562–8573.

46 P. Chevallier, A. Walter, A. Garofalo, I. Veksler, J. Lagueux, S. Bégin-Colin, D. Felder-Flesch and M.-A. Fortin, *J. Mater. Chem. B*, 2014, **2**, 1779.

47 A. Walter, C. Billotey, A. Garofalo, C. Ulhaq-Bouillet, C. Lefèvre, J. Taleb, S. Laurent, L. Vander Elst, R. N. Muller, L. Lartigue, F. Gazeau, D. Felder-Flesch and S. Begin-Colin, *Chem. Mater.*, 2014, **26**, 5252–5264.

48 A. Walter, A. Garofalo, P. Bonazza, F. Meyer, H. Martinez, S. Fleutot, C. Billotey, J. Taleb, D. Felder-Flesch and S. Begin-Colin, *ChemPlusChem*, 2017, **82**, 647–659.

49 J. Rodríguez-Carvajal, *Phys. B*, 1993, **192**, 55–69.

50 A. Le Bail, H. Duroy and J. L. Fourquet, *Mater. Res. Bull.*, 1988, **23**, 447–452.

51 J. Teillet and F. Varret, Unpublished MOSFIT Program, n.d.

52 B. Mehdaoui, J. Carrey, M. Stadler, A. Cornejo, C. Nayral, F. Delpech, B. Chaudret and M. Respaud, *Appl. Phys. Lett.*, 2012, **100**, 052403.

53 K. Fabian, *Phys. Earth Planet. Inter.*, 2006, **154**, 299–307.

54 G. E. P. Box and H. L. Lucas, *Biometrika*, 1959, **46**, 77–90.

55 G. Cotin, C. Kiefer, F. Perton, M. Boero, B. Özdamar, A. Bouzid, G. Ori, C. Massobrio, D. Begin, B. Pichon, D. Mertz and S. Begin-Colin, *ACS Appl. Nano Mater.*, 2018, **1**, 4306–4316.

56 G. Cotin, F. Perton, C. Petit, S. Sall, C. Kiefer, V. Begin, B. Pichon, C. Lefevre, D. Mertz, J.-M. Greneche and S. Begin-Colin, *Chem. Mater.*, 2020, **32**, 9245–9259.

57 E. Wetterskog, C.-W. Tai, J. Grins, L. Bergström and G. Salazar-Alvarez, *ACS Nano*, 2013, **7**, 7132–7144.

58 A. Lak, M. Cassani, B. T. Mai, N. Winckelmans, D. Cabrera, E. Sadrollahi, S. Marras, H. Remmer, S. Fiorito, L. Cremades-Jimeno, F. J. Litterst, F. Ludwig, L. Manna, F. J. Teran, S. Bals and T. Pellegrino, *Nano Lett.*, 2018, **18**, 6856–6866.

59 B. P. Pichon, O. Gerber, C. Lefevre, I. Florea, S. Fleutot, W. Baaziz, M. Pauly, M. Ohlmann, C. Ulhaq, O. Ersen, V. Pierron-Bohnes, P. Panissod, M. Drillon and S. Begin-Colin, *Chem. Mater.*, 2011, **23**, 2886–2900.

60 E. Wetterskog, C.-W. Tai, J. Grins, L. Bergström and G. Salazar-Alvarez, *ACS Nano*, 2013, **7**, 7132–7144.

61 C. Bordeianu, A. Parat, C. Affolter-Zbaraszczuk, R. N. Muller, S. Boutry, S. Begin-Colin, F. Meyer, S. Laurent and D. Felder-Flesch, *J. Mater. Chem. B*, 2017, **5**, 5152–5164.

62 T. J. Daou, G. Pourroy, J. M. Greneche, A. Bertin, D. Felder-Flesch and S. Begin-Colin, *Dalton Trans.*, 2009, 4442–4449.

63 A. Mitra, J. Mohapatra, S. S. Meena, C. V. Tomy and M. Aslam, *J. Phys. Chem. C*, 2014, **118**, 19356–19362.

64 Ö. Özdemir, D. J. Dunlop and T. S. Berquó, *Geochem., Geophys., Geosyst.*, 2008, **9**, Q10Z01.

65 F. Bødker and S. Mørup, *Europhys. Lett.*, 2000, **52**, 217–223.

66 W. Baaziz, B. P. Pichon, S. Fleutot, Y. Liu, C. Lefevre, J.-M. Greneche, M. Toumi, T. Mhiri and S. Begin-Colin, *J. Phys. Chem. C*, 2014, **118**, 3795–3810.

67 D. Ortega, M. V. Kuznetsov, Y. G. Morozov, O. V. Belousova and I. P. Parkin, *Phys. Chem. Chem. Phys.*, 2013, **15**, 20830–20838.

68 T. M. de L. Alves, B. F. Amorim, M. A. M. Torres, C. G. Bezerra, S. N. de Medeiros, P. L. Gastelois, L. E. F. Outon and W. A. de A. Macedo, *RSC Adv.*, 2017, **7**, 22187–22196.

69 F. Bødker, M. F. Hansen, C. B. Koch, K. Lefmann and S. Mørup, *Phys. Rev. B: Condens. Matter Mater. Phys.*, 2000, **61**, 6826–6838.

70 H. Kachkachi and M. Dimian, *Phys. Rev. B: Condens. Matter Mater. Phys.*, 2002, **66**, 174419.

71 D. Cabrera, A. Lak, T. Yoshida, M. E. Materia, D. Ortega, F. Ludwig, P. Guardia, A. Sathya, T. Pellegrino and F. J. Teran, *Nanoscale*, 2017, **9**, 5094–5101.

72 I. Morales, R. Costo, N. Mille, G. B. Da Silva, J. Carrey, A. Hernando and P. De la Presa, *Nanomaterials*, 2018, **8**, 970.

73 A. Demortière, P. Panissod, B. P. Pichon, G. Pourroy, D. Guillon, B. Donnio and S. Bégin-Colin, *Nanoscale*, 2011, **3**, 225–232.

74 A. Walter, C. Billotey, A. Garofalo, C. Ulhaq-Bouillet, C. Lefèvre, J. Taleb, S. Laurent, L. Vander Elst, R. N. Muller, L. Lartigue, F. Gazeau, D. Felder-Flesch and S. Begin-Colin, *Chem. Mater.*, 2014, **26**, 5252–5264.

75 M. V. Rastei, V. Pierron-Bohnes, D. Toulemon, C. Bouillet, A. Kákay, R. Hertel, E. Tetsi, S. Begin-Colin and B. P. Pichon, *Adv. Funct. Mater.*, 2019, **29**, 1903927.

76 A. Roch, P. Gillis, A. Ouakssim and R. N. Muller, *J. Magn. Magn. Mater.*, 1999, **201**, 77–79.

77 R. Hergt and S. Dutz, *J. Magn. Magn. Mater.*, 2007, **311**, 187–192.

78 S. B. Nielsen, K. Wilhelm, B. Vad, J. Schleucher, L. A. Morozova-Roche and D. Otzen, *J. Mol. Biol.*, 2010, **398**, 351–361.

79 C.-W. Lu, Y. Hung, J.-K. Hsiao, M. Yao, T.-H. Chung, Y.-S. Lin, S.-H. Wu, S.-C. Hsu, H.-M. Liu, C.-Y. Mou, C.-S. Yang, D.-M. Huang and Y.-C. Chen, *Nano Lett.*, 2007, **7**, 149–154.

80 A. Walter, A. Garofalo, A. Parat, H. Martinez, D. Felder-Flesch and S. Bégin-Colin, *Nanotechnol. Rev.*, 2015, **4**, 581.

81 A. Walter, A. Garofalo, A. Parat, J. Jouhannaud, G. Pourroy, E. Voirin, S. Laurent, P. Bonazza, J. Taleb, C. Billotey, L. V. Elst, R. N. Muller, S. Begin-Colin and D. Felder-Flesch, *J. Mater. Chem. B*, 2015, **3**, 1484–1494.

82 P. Guardia, A. Riedinger, S. Nitti, G. Pugliese, S. Marras, A. Genovese, M. E. Materia, C. Lefevre, L. Manna and T. Pellegrino, *J. Mater. Chem. B*, 2014, **2**, 4426.

83 F. H. L. Starsich, C. Eberhardt, A. Boss, A. M. Hirt and S. E. Pratsinis, *Adv. Healthcare Mater.*, 2018, **7**, 1800287.

84 E. D. Smolensky, H.-Y. E. Park, Y. Zhou, G. A. Rolla, M. Marjańska, M. Botta and V. C. Pierre, *J. Mater. Chem. B*, 2013, **1**, 2818.

85 J.-H. Lee, Y.-M. Huh, Y. Jun, J. Seo, J. Jang, H.-T. Song, S. Kim, E.-J. Cho, H.-G. Yoon, J.-S. Suh and J. Cheon, *Nat. Med.*, 2007, **13**, 95–99.

86 H. M. Joshi, Y. P. Lin, M. Aslam, P. V. Prasad, E. A. Schultz-Sikma, R. Edelman, T. Meade and V. P. Dravid, *J. Phys. Chem. C*, 2009, **113**, 17761–17767.

87 N. Lee, Y. Choi, Y. Lee, M. Park, W. K. Moon, S. H. Choi and T. Hyeon, *Nano Lett.*, 2012, **12**, 3127–3131.

88 Z. Zhou, R. Tian, Z. Wang, Z. Yang, Y. Liu, G. Liu, R. Wang, J. Gao, J. Song, L. Nie and X. Chen, *Nat. Commun.*, 2017, **8**, ncomms15468.

89 S. Noh, W. Na, J. Jang, J.-H. Lee, E. J. Lee, S. H. Moon, Y. Lim, J.-S. Shin and J. Cheon, *Nano Lett.*, 2012, **12**, 3716–3721.

90 Q. Song and Z. J. Zhang, *J. Am. Chem. Soc.*, 2004, **126**, 6164–6168.

91 P. Guardia, R. Di Corato, L. Lartigue, C. Wilhelm, A. Espinosa, M. Garcia-Hernandez, F. Gazeau, L. Manna and T. Pellegrino, *ACS Nano*, 2012, **6**, 3080–3091.

92 P. Guardia, A. Labarta and X. Batlle, *J. Phys. Chem. C*, 2011, **115**, 390–396.

93 D. J. Dunlop and Ö. Özdemir, *Rock Magnetism: Fundamentals and Frontiers*, Cambridge University Press, 2001.